Authors accepted copy. Please cite as: I. Tari, M. Mehrtash / International Journal of Heat and Mass Transfer 56 (2013) 574–593

# NATURAL CONVECTION HEAT TRANSFER FROM INCLINED PLATE-FIN HEAT SINKS

Ilker Tari[1], Mehdi Mehrtash

Mechanical Engineering Department, Middle East Technical University, 06800 Ankara, Turkey

**Abstract**
The steady-state natural convection from heat sinks with parallel arrangement of rectangular cross section vertical plate fins on a vertical base are numerically investigated in order to obtain a validated model that is used for investigating inclined orientations of a heat sink. Taking a previous experimental study as a basis, aluminum heat sinks with two different practical lengths are modeled. The models and the simulation approach are validated by comparing the flat plate heat sink results with the available correlations, and by comparing the finned heat sink results with the experimental data. Natural convection and radiation heat transfer rates from the fronts of the heat sinks heated from the back with a heater are obtained from finite volume computational fluid dynamics simulations. The sensitivities of the heat transfer rates to the geometric parameters are determined. A set of dimensionless correlations for the convective heat transfer rate is suggested. The validated model is used for several upward and downward inclination angles by varying the direction of gravitational acceleration. At small inclinations, it is observed that convection heat transfer rate stays almost the same, even increases slightly for the downward inclinations. At larger angles, the phenomenon is investigated for the purpose of determining the flow structures forming around the heat sink. For the inclination angles of ±4°, ±10°, ±20°, ±30°, ±45°, ±60°, ±75°, +80°, ±85°, ±90° from the vertical, the extent of validity of the obtained vertical case correlation is investigated by modifying the Grashof number with the cosine of the inclination angle. It is observed that the correlation is valid in a very wide range, from −60° (upward) to +80° (downward). It is also observed that the flow separation inside the fin channels of the heat sink is an important phenomenon and determines the validity range of the modified correlation. It is further shown that the correlations are also applicable to all available inclined case data in the literature, verifying both our results and correlations. Since the investigated ranges of parameters are suitable for electronic device cooling, the suggested correlations have a practical use in electronics cooling applications.

*Keywords:* Plate fin array; Vertical heat sink; Inclined heat sink; Natural convection; Electronics cooling.

## Nomenclature

| | |
|---|---|
| $c_p$ | Heat capacity, J/K |
| $d$ | Base plate thickness, mm |
| $g$ | Gravitational acceleration, m/s$^2$ |
| $Gr'$ | Modified Grashof number, $Gr' = [g\beta\Delta T S^4]/[\nu^2 (LH)^{0.5}]$ |

[1] Corresponding author. Tel.: +90 312 2102551; fax: +90 312 2102536. E-mail address: itari@metu.edu.tr (I. Tari).

| | |
|---|---|
| $h$ | Average heat transfer coefficient, W/(m$^2$ K) |
| $H$ | Fin height, mm |
| $k$ | Thermal conductivity of fluid (air), W/(m K) |
| $L$ | Fin length, mm |
| $\overline{Nu_L}$ | Average Nusselt number based on L, $\overline{Nu_L} = (hL)/k$ |
| $\overline{Nu_S}$ | Average Nusselt number based on $S$, $\overline{Nu_S} = (hS)/k$ |
| $p$ | Pressure, atm |
| $P$ | Non-dimensional pressure |
| $Pr$ | Prandtl number |
| $Q_c$ | Convection heat transfer rate from fin array, W |
| $Q_{in}$ | Power supplied to heater plate, W |
| $Q_r$ | Radiative heat transfer rate from fin array, W |
| $Ra$ | Rayleigh number based on $L$, $Ra = g\beta L^3(T_w - T_a)/(\nu\alpha)$ |
| $S$ | Fin spacing, mm |
| $S_{opt}$ | Optimum fin spacing, mm |
| $t$ | Fin thickness, mm |
| $T_w$ | Average base wall temperature, ºC |
| $T_a$ | Ambient temperature, ºC |
| $T$ | Temperature, ºC |
| $T_f$ | Film temperature, ºC |
| $\Delta T$ | Base-to-ambient temperature difference, K |
| $W$ | Heat sink width, mm |
| $u, v, w$ | Velocities in $x$, $y$ and $z$ directions |
| $v', w'$ | Characteristic velocities in $y$ and $z$ directions |
| $\mathcal{V}, \mathcal{W}$ | Non-dimensional velocities in $y$ and $z$ directions |
| $x, y, z$ | Cartesian coordinates |
| $X, Y, Z$ | Non-dimensional coordinates |

*Greek Symbols*

| | |
|---|---|
| $\alpha$ | Thermal diffusivity, m$^2$/s |
| $\beta$ | Volumetric thermal expansion coefficient, 1/K |
| $\varepsilon$ | Emissivity |
| $\theta$ | Angle of inclination with respect to vertical position, degrees |
| $\mu$ | Dynamic viscosity, s/m$^2$ |
| $\rho$ | Density, kg/m$^3$ |
| $\nu$ | Kinematic viscosity, m$^2$/s |
| $\phi$ | Non-dimensional temperature |

## 1. Introduction

Heat sinks with extended surfaces have been widely used in various engineering applications especially in electronics cooling. Due to ease of manufacturing, parallel arrangement of rectangular cross section plate fins on a flat base is the most common heat sink geometry. Heat sinks with this geometry have been used for both forced and natural convection. In the case of forced convection, the geometric parameters of a heat sink highly depend on the remaining components of the cooling system, such as the fan and the enclosure; therefore, the optimal values of these parameters depend on the considered application. In contrast, in natural convection, it is possible to optimize the parameters of the heat sink geometry in an application independent manner. Consequently, in literature, there are several attempts for optimizing parameters in the case of natural convection for vertical and horizontal orientations of the heat sink. However, the suggested correlations for the optimal values of the geometric parameters and for possible natural convection heat transfer rates considerably vary among different studies; these attempts do not converge to a consistent set of correlations.

The objective of the present study is to obtain a consistent set of correlations for all orientations of plate-fin heat sinks, including the vertical. At the end of the study, our efforts converge to a single correlation covering a wide range of angles between vertical and horizontal orientations in both upward and downward facing directions of the heat sink. The suggested correlation agrees very well with all available experimental data in literature for the inclined case (Mittelmann *et al.* [1] and Starner and McManus [2], with %5.8 and %8.8 mean relative errors, respectively).

Heat sinks with parallel arrangement of rectangular cross section plate fins on a flat base are used preferably in vertical or upward facing horizontal orientations in order to obtain higher natural convection rates [2]. In certain scenarios, however, these two orientations may not be suitable due to several system related constraints, *e.g.*, lack of available space on the side and top surfaces of the electronic box or lack of any vertical or horizontal surface in the design. Moreover, one may be forced to use plate-fin heat sinks in inclined orientations when a vertical or horizontal heat sink is inclined due to a rotation of the device. These possible scenarios motivate this study.

In practice, there is certainly a need for investigating inclined plate-fin heat sinks. For example, when natural convection with vertical plate-fin heat sinks was suggested as a viable solution for cooling of flat panel displays with high power components [3] and of laptop computers [4], the major concern was how to handle the situation if the device is operated when the heat sink is inclined due to the inclination of the screen.

Even though there are several studies investigating natural convection heat transfer from vertical plate fins protruding from a vertical base [5-14] or from a horizontal base [15-21], Mittelmann *et al.* [1] and Starner and McManus [2] are the only ones investigating inclined orientations of plate-fin heat sinks. The ranges of the parameters investigated in the previous works are summarized in Table 1, together with the ones for the present work (the last row). The last column in Table 1 shows the investigated inclination angles from the vertical, where the zero corresponds to the vertical orientation of the base while upward inclinations are negative. Notice that Starner and McManus [2] deals only with upward 45° inclination, and Mittelman *et al.* [1] with downward inclination angles between 60° and 90°. The present study, by investigating wide range of upward and downward angles, fills a gap in literature.

Firstly, we consider the vertical case, for which extensive experimental data is available for numerical model validation. Secondly, upon validating our numerical model and suggesting a set of correlations for the vertical case, we use both the model and the correlations to investigate the inclined case. Since there is practical motivation for studying inclined orientations for electronics cooling applications, the size of the simulated heat sink is selected accordingly.

## 2. Numerical Model and Method

A recent experimental study, Yazicioğlu and Yüncü [13,14], is taken as the base case for the validation of our vertical model. The experimental set-up is numerically modeled and simulations are performed for the same set of parameters, using the information presented in [14]. The simulation results are compared with the experimental heat sink temperatures in order to verify that the simulations are representing the conditions of the experiments. The data in [14] together with the data from literature ([2,7,8,9] for the vertical and [1,2] for the inclined cases) are used for comparison and verification.

Table 1 Ranges of parameters investigated in the literature

| **Reference** | **Fin Length** ***L*** **(mm)** | **Base Width** ***W*** **(mm)** | **Fin Height** ***H*** **(mm)** | **Fin Thickness** ***t*** **(mm)** | **Fin Spacing** ***S*** **(mm)** | **Base-to-Ambient Temperature Difference** $\Delta T$ **(°C)** | **Optimum Fin Spacing** $S_{opt}$ **(mm)** | **Angle from Vertical** $\theta$ **(deg)** |
|---|---|---|---|---|---|---|---|---|
| [1] | 200 | 130 | 21.5-34 | 1.1 | 7-17 | 16.4-55.6 | - | 60,70,80,90 |
| [2] | 127 | 254 | 6.35-25.4 | 1.02 | 6.35-7.95 | 25-90 | - | 0,-45,-90 |
| [6] | 203 | 66.3 | 6.35-19.05 | 2.3 | 4.8-19 | 35-90 | - | 0 |
| [7] | 150 | 190 | 10, 17 | 3 | 3-45 | 20-40 | 9, 9.5 | 0,-90 |
| [8] | 250 | 190 | 60 | 3 | 3-33 | 20-80 | 9-11 | 0,-90 |
| [9] | 150, 250, 375, 500 | 190 | 30, 60, 90 | 1-19 | 3-76 | 20-40 | 9.5-11 | 0 |
| [10] | 150, 250, 375, 500 | 190 | 30, 60, 90 | 1-19 | 3-76 | 20-40 | 9.5-11 | 0 |
| [11] | 100 | 250 | 5-25 | 3 | 5-34 | 14-106 | 7 | 0 |
| [12] | 25-49 | 25-49 | 13.5 | 1 | 3-11 | 15-22 | - | 0 |
| [13] [14] | 250, 340 | 180 | 5-25 | 3 | 5-85.5 | 21-162 | 11.2 | 0 |
| [15] | 130-390 | 130 | 10.5-34 | 1.1 | 7 | 16-76 | 6-11 | 90 |
| [16] | 500 | 190 | 60 | 3 | 5-77 | 20-40 | 12 | 0,-90 |
| [17] | 100 | 250 | 6-26 | 3 | 6.2-83 | 13-133 | 10.5-20 | -90 |
| [18] | 100 | - | 5-35 | - | 5-20 | 36-96 | - | -90 |
| [19] | 127-381 | - | 6.3-50 | - | 4-38.1 | 33-100 | - | -90 |
| [20] | 127-381 | - | 26-47 | - | 4-38.1 | 20-70 | - | -90 |
| [21] | 7-50 | - | 7-12 | 3-7 | 4-12 | 40-60 | - | -90 |
| Present | 250, 340 | 180 | 5-25 | 3 | 5-85.5 | 14-185 | 11.75 | 0,±4,±10,±20, ±30,±45,±60, ±75,+80, ±85,±90 |

The experimental set-up in [14] consists of a heat sink installed on the front of a heater plate with layers of insulation in the back. The experiments have been performed in a small room with nearly stagnant air and nearly constant temperature. In our model, the backside insulation of the heater plate is simplified and replaced with an equivalent aerated concrete block (see Fig. 1). The assembly in Fig. 1 is placed in an air filled cubical room of 3 m sides with walls that are kept at uniform 20 °C, as shown in Fig. 2. The properties of the model components are given in Table 2. The technical drawings of two investigated heat sinks with their dimensions are shown in Fig. 3. The six locations marked on each heat sink base are the locations of the thermocouples in the experiments. These locations are used in our simulations for convergence monitoring and comparisons with the experimental temperature data.

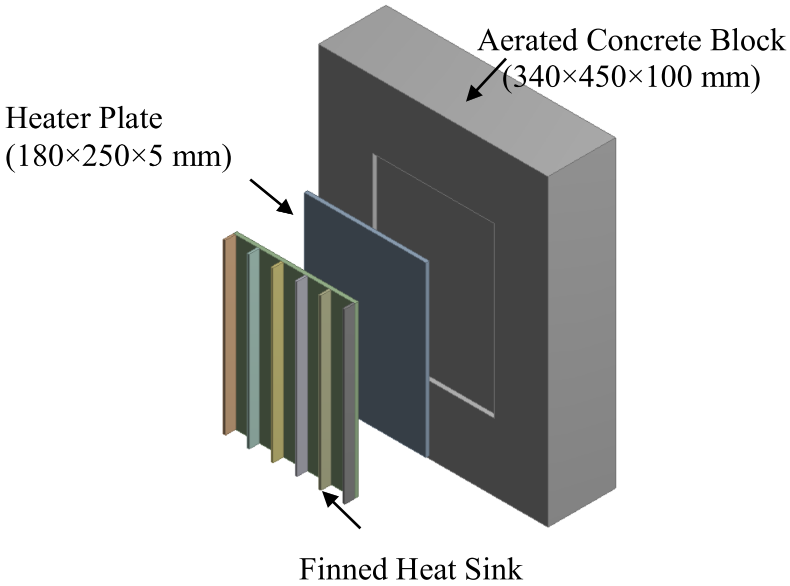


Fig. 1. Schematic view of the model for the heat sink length of 250 mm.

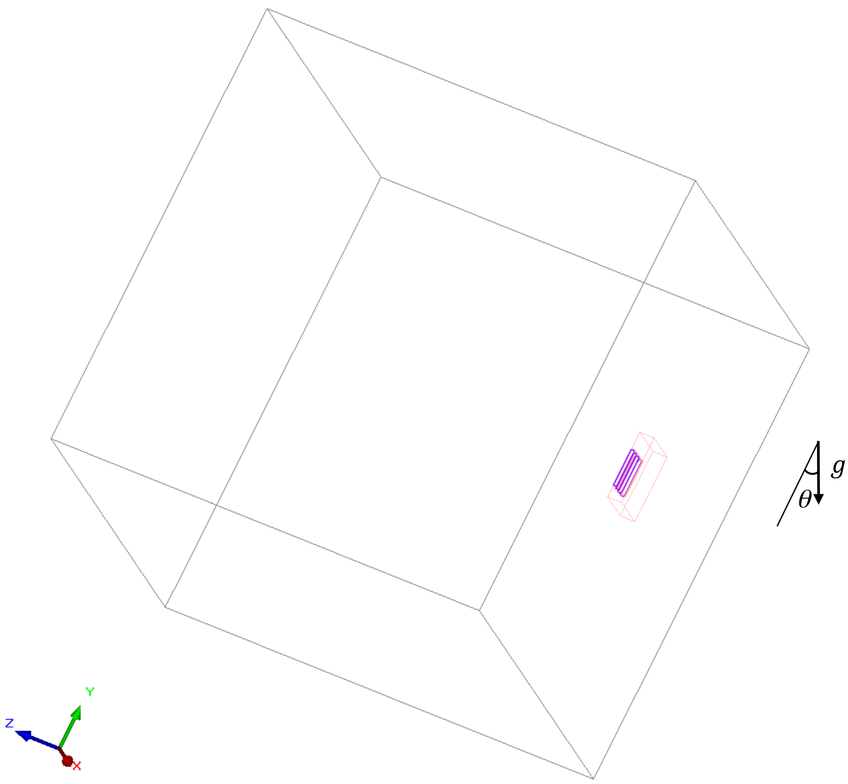


Fig. 2. The 3D view of the computational domain. The domain is inclined with the angle $\boldsymbol{\theta}$ by changing the direction of the gravitational acceleration $g$.

Table 2 Properties of the components

| Component | Material Type | Specific Heat (J/kg K) | Conductivity (W/m K) | Emissivity | Roughness (mm) |
|---|---|---|---|---|---|
| Concrete Block | Aerated Concrete | 1000 | 0.15 | 0.9 | 2 |
| Heater Base Plate | Aluminum | 900 | 130 | 0.2 | 0.02 |
| Fin array | Aluminum | 900 | 130 | 0.2 | 0.02 |

In order to simulate experimental cases as closely as possible, the dimensions of the aerated concrete insulation are determined after several trials of matching the heat sink surface temperatures to the experimental results at the thermocouple locations.

Steady state solutions are obtained by using the zero-equation-turbulence model with initial ambient air temperature of 20 °C. Air is taken as an ideal gas at atmospheric pressure. No slip boundary condition is used for all surfaces. There is no contact resistance between solid surfaces.

A non-conformal mesh structure with a very fine grid around the cooling assembly and a coarse grid for the rest of the room is employed. Grid independence is achieved by examining three different grid densities with 1685832, 2834264 and 4077608 cells, and then selecting the medium density mesh, *i.e.*, the one with 2834264 cells, as it yields results matching to those of the fine mesh.

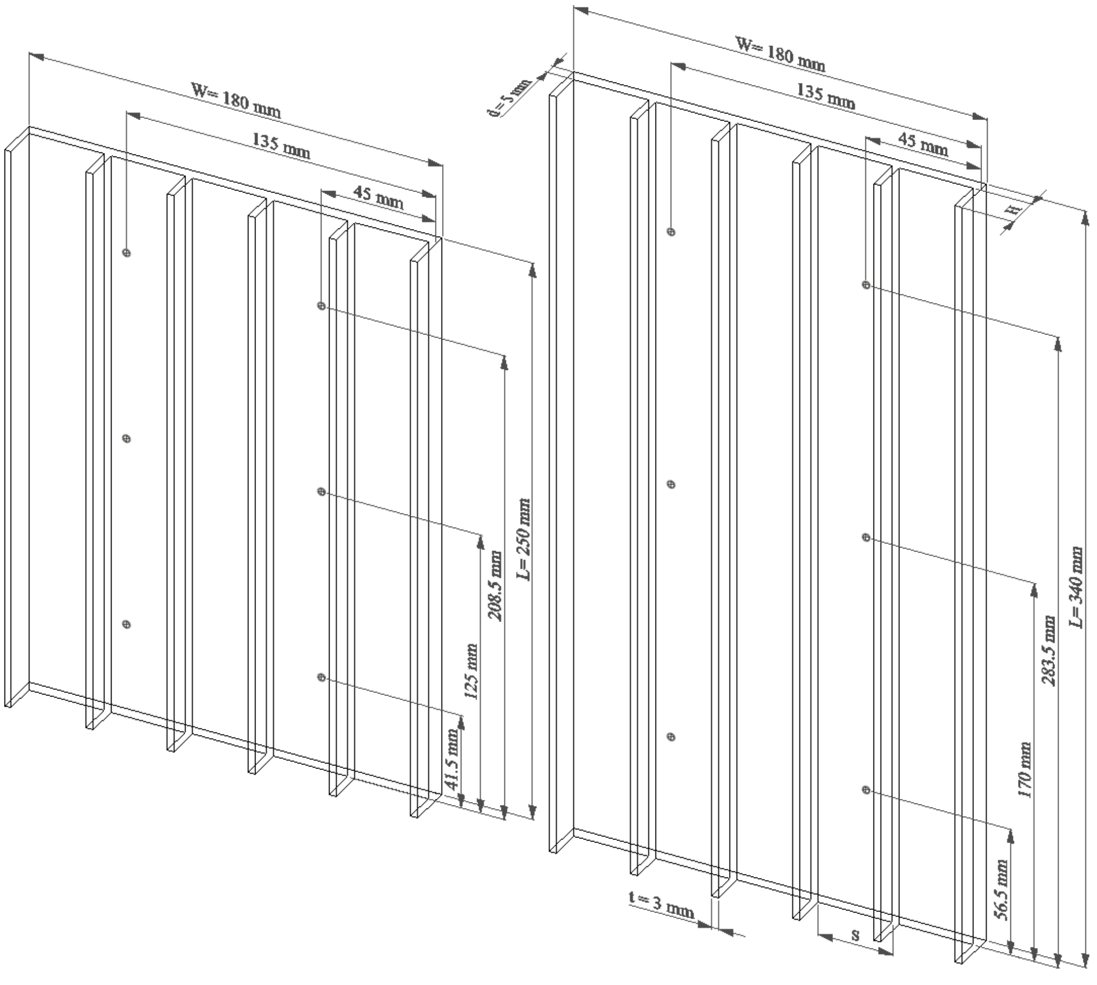


Fig. 3. Locations of the six temperature monitoring points (thermocouple positions) together with the dimensions of the heat sinks.

ANSYS Fluent solver [22] is used for solving the continuity, momentum and thermal energy equations for air and the heat conduction equation within the solids. To handle the radiative heat transfer, the surface-to-surface radiation model is used.

*2.1 Vertical Model Validation*

The model, mesh and solution parameters are validated by comparing the simulation results with the results from available empirical correlations after replacing the finned heat sink with a flat plate. Considered correlations are
*Mc Adam's relation* [23],

$$\overline{Nu_L} = 0.59\ Ra^{1/4} \tag{1}$$

*Churchill and Chu's first relation* [24],

$$\overline{Nu_L} = \left[0.825 + \frac{0.387\ Ra^{1/6}}{[1 + (0.492/Pr)^{9/16}]^{8/27}}\right]^2 \tag{2}$$

*Churchill and Chu's second relation* [24],

$$\overline{Nu_L} = 0.68 + \frac{0.67\ Ra^{1/4}}{[1 + (0.492/Pr)^{9/16}]^{4/9}} \tag{3}$$

In Eqs (1)-(3), the Rayleigh number is defined based on the heat sink length $L$ as $Ra = g\beta L^3(T_w - T_a)/(\nu\alpha)$ in which $g$ is the gravitational acceleration, $T_w$ and $T_a$ are respectively the wall and ambient air temperatures, and $\beta$, $\nu$, $\alpha$ and $Pr$ are the properties of air.

The comparison is given in Table 3. The agreement of the results especially with Eq. (3) is very good (with 5.1% average relative error). This is an indication of sufficient grid structure and suitable modeling approach. In addition to the flat plate case, the numerical temperature results are compared at every step with the available experimental results showing a very good agreement.

Table 3 Comparison of Nusselt numbers for vertical flat plate case with the correlations from literature

| | | Average $Nu_L$ | | | |
|---|---|---|---|---|---|
| ***$Q_{in}$ (W)*** | ***Ra*** | **McAdam's relation** | **Churchill and Chu's first relation** | **Churchill and Chu's second relation** | **Present Study** |
| 20 | 4.86E+07 | 49.26 | 49.26 | 43.58 | 45.59 |
| 30 | 6.08E+07 | 52.11 | 52.63 | 46.05 | 48.33 |
| 40 | 6.85E+07 | 53.68 | 54.51 | 47.42 | 49.92 |
| 50 | 7.36E+07 | 54.66 | 55.67 | 48.25 | 50.83 |
| 60 | 7.78E+07 | 55.41 | 56.57 | 48.91 | 51.53 |
| 70 | 8.01E+07 | 55.82 | 57.06 | 49.25 | 51.99 |
| 80 | 8.17E+07 | 56.09 | 57.37 | 49.48 | 52.16 |
| 90 | 8.27E+07 | 56.26 | 57.55 | 49.61 | 52.48 |
| 100 | 8.29E+07 | 56.30 | 57.59 | 49.63 | 52.29 |
| 110 | 8.28E+07 | 56.29 | 57.57 | 49.62 | 52.45 |

| | | | | | |
|---|---|---|---|---|---|
| 120 | 8.25E+07 | 56.23 | 57.48 | 49.56 | 52.28 |
| 130 | 8.20E+07 | 56.15 | 57.37 | 49.48 | 52.25 |
| 140 | 8.14E+07 | 56.05 | 57.23 | 49.38 | 52.09 |

### *2.2 Convective heat transfer rate*

In [14] Yazicioğlu used a calibration that replaces the heat sink with an assembly of two identical parallel flat plates separated by a very small distance (two-flat-plate-case) so that the front heat transfer is only due to the radiative transfer between the plates (by neglecting the heat conduction through the thin air layer), giving a conductive heat loss value from the backside using the knowledge of the input power to the heater. When the actual finned heat sink is installed, he assumed that the fraction of heat loss from the back stays the same as the two-flat-plate-case.

We believe that his assumption is not correct because a finned heat sink is expected to transfer higher fractional heat rate from the front as compared to a flat plate, causing a lower fraction of heat loss from the back. In our opinion, he should have used a guard heater to compensate for the backside heat losses following the same path in most of the similar studies in literature [1][2][6]-[10], or a heat sink structure that is symmetrical on both sides eliminating the need for insulation as it was done in [5].

Nevertheless, we believe that the temperature measurements in [14] are still correct. Therefore, we calibrate our insulation thickness to get temperature results matching the temperature measurements in [14]. By this way, we replicate the experimental case and at the same time we can estimate the backside conductive loss and convective heat transfer rates from the front side of the vertical plate-fin heat sink directly from our simulations. Notice that due to the aforementioned problem, in our opinion, the convective heat transfer rates calculated in [14] are underestimates, as shown in Table 4.

### *2.3 Optimum fin spacing*

There is an optimum fin spacing maximizing the heat transfer rate from the heat sink for each heater input power, thus, minimizing the average heat sink temperature. To determine this optimum fin spacing, the approach followed in both [8] and [14] is adopted. The optimization approach consists of three steps: trying several fin spacing values sampled from the interval bounded by the small-$S$ and large-$S$ limits, drawing asymptotes from both left (small-$S$ limit) and right (large $S$-limit), and identifying the spacing corresponding to the intersection of the asymptotes as the optimum value, $S_{opt}$.

### *2.4 Other parameters affecting heat sink performance*

In addition to the fin spacing ($S$), the main geometric factors affecting the performance of a plate-fin heat sink are the heat sink length ($L$) and the fin height ($H$). The fin thickness ($t$) is taken as constant throughout the simulations because it only affects the conduction resistance inside the fins; the selected thickness value, which is 3 mm, is enough to guarantee that overall surface efficiencies are nearly equal to one. Similarly, the base thickness ($d$) is also kept constant. Two different lengths (250 and 340 mm), three different fin heights (5, 15 and 25 mm) and five different fin spacing values (5.85, 8.8, 14.7, 32.4 and 85.5 mm) are investigated for five heater input powers (25, 50, 75, 100 and 125 W).

Table 4 The present estimates (sim) and the calculated ones in Ref. [14] of convective heat transfer rate ($Q_c$) for $L$=250 mm.

| Fin height $H$ (mm) | Fin spacing $S$ (mm) | Number of Fins | Convective heat transfer rate, $Q_c$ (W) | | | | | | | | | |
|---|---|---|---|---|---|---|---|---|---|---|---|---|
| | | | $Q_{in}$=25 W | | $Q_{in}$ =50 W | | $Q_{in}$ =75 W | | $Q_{in}$ =100 W | | $Q_{in}$ =125 W | |
| | | | sim | [14] | sim | [14] | sim | [14] | sim | [14] | sim | [14] |
| 25 | 85.5 | 3 | 16.41 | 10.01 | 33.77 | 20.89 | 51.09 | 30.72 | 68.16 | 40.61 | 84.91 | 50.75 |
| 25 | 32.4 | 6 | 17.54 | 10.57 | 36.09 | 21.45 | 54.68 | 31.67 | 73.13 | 42.39 | 90.9 | 52.96 |
| 25 | 14.7 | 11 | 18.33 | 10.13 | 37.96 | 21 | 57.7 | 31.68 | 77.42 | 43.15 | 97.45 | 54.81 |
| 25 | 8.8 | 16 | 17.85 | 9.9 | 37.4 | 20.93 | 57.18 | 31.82 | 76.99 | 43.04 | 94.52 | 53.78 |
| 25 | 5.85 | 21 | 16.87 | 9.45 | 35.61 | 19.85 | 54.63 | 30.36 | 73.67 | 40.93 | 92.63 | 51.25 |
| 15 | 85.5 | 3 | 15.79 | 10.31 | 32.53 | 20.62 | 49.16 | 30.56 | 65.51 | 39.54 | 81.49 | 49.08 |
| 15 | 32.4 | 6 | 16.66 | 10.01 | 34.34 | 20.31 | 52.02 | 30.06 | 69.52 | 39.89 | 86.74 | 50.13 |
| 15 | 14.7 | 11 | 17.41 | 9.96 | 36.07 | 20.26 | 54.81 | 31.12 | 73.45 | 41.45 | 91.91 | 51.49 |
| 15 | 8.8 | 16 | 17 | 9.47 | 35.57 | 19.85 | 54.31 | 30.5 | 72.99 | 40.65 | 91.53 | 50.07 |
| 15 | 5.85 | 21 | 16.18 | 9.16 | 34.07 | 18.99 | 52.12 | 28.54 | 70.07 | 38.88 | 87.86 | 48.14 |
| 5 | 85.5 | 3 | 14.82 | 10.33 | 30.54 | 20.49 | 46.1 | 30.3 | 61.37 | 39.59 | 76.17 | 48.74 |
| 5 | 32.4 | 6 | 15.11 | 10.02 | 31.23 | 20.39 | 47.2 | 30.13 | 62.84 | 39.41 | 78.09 | 48.7 |
| 5 | 14.7 | 11 | 15.47 | 10.14 | 32.05 | 20.2 | 48.56 | 30.36 | 64.77 | 39.51 | 81.14 | 49.2 |
| 5 | 8.8 | 16 | 15.37 | 9.7 | 32.02 | 19.8 | 48.39 | 29.49 | 64.97 | 39.02 | 81 | 48.37 |
| 5 | 5.85 | 21 | 15 | 9.3 | 31.35 | 18.82 | 47.65 | 28.08 | 63.66 | 36.85 | 79.28 | 45.39 |

### *2.5 Acquisition of data from literature*

The data from older works in literature, of which data is not available, is obtained by digitizing the figures in each one of them. Digitization error depends on the figure quality as well as the value of the data point. Using the ground truth from recent works, we estimated the digitization error as 1%. For Leung *et al.* data [7,8,9], for which the ground truth is not available, we obtained an estimate of the digitization error as 2.5% by comparing the digitized $x$-axis values obtained from $Q/WL$ versus $S$ figures with the reported values of fin spacing ($S$) given as investigated range.

### *2.6 Statistical analysis of the data*

While statistically analyzing the simulation data we consider both the classical least squares approach and robust approach using Huber and Tukey [25] norms for measuring deviations from the fit. Since all of the fits are nonlinear (power fit), the squared correlation coefficients $R^2$, measuring goodness of fit, are calculated using the following formula:

$$R^2 = 1 - \frac{MSE\ (n-1)}{\sum(y-\bar{y})^2} \tag{4}$$

where $MSE$ is the mean squared error, $n$ is the sample size, and $\bar{y}$ is the average of $y$.

For all of the three fitting approaches, we report both $R^2$ values and 95% confidence intervals for estimated parameters (Appendix).

### *2.7 Inclined heat sink*

We directly use the approach (the model, the mesh and the solution scheme) that is validated for the vertical case by varying the direction of the gravitational acceleration ($g$) in order to create the effect of inclination without changing any of the validated model parameters. This approach makes the room to rotate with the heat sink (see Fig. 2). Since the heat sink is very small compared to the large air volume of the computational domain (the room) and placed at the center of one of the identical walls, and since all of the walls of the cubical room are at the same uniform temperature, changing the direction of $g$ does not affect the air circulation within the room away from the heat sink (in the far field) while affecting the air circulation only in the vicinity of the heat sink (in the near field), thus creating the desired effect. It is confirmed with the simulation results that the far field air flow does not change with the inclination and air always returns to the heat sink at 20 °C.

For the fin spacing of 11.75 mm by equally spacing 13 fins and fixing the length to 250 mm, steady state solutions are obtained for the inclination angles of ±4°, ±10°, ±20°, ±30°, ±45°, ±60°, ±75°, +80°, ±85°, ±90° from the vertical. Three different heater input power values ($Q_{in}$) of 25, 75 and 125 W are investigated.

## 3. Results and discussion

Simulations are run until convergence of the temperature values at six thermocouple locations (marked in Fig. 3). During the post processing, the average of these temperatures is taken as the wall temperature ($T_w$). Considering that the room (the computational domain) is very large compared to the heat sink and the walls of the room are maintained at 20 °C, ambient air temperature ($T_a$) is taken as 20 °C. The heat sink base-to-ambient temperature difference is defined as $\Delta T = T_w - T_a$. For evaluating the properties of air, the film temperature ($T_f$) is defined as the average of $T_w$ and $T_a$.

The convective heat transfer rate from the heat sink ($Q_c$) is determined by subtracting the radiative transfer rate of the heat sink ($Q_r$) from its total heat transfer rate, both being obtained from the simulation results.

In Subsections 3.1-3.3, we report our observations related to effects of heat sink geometric parameters on the flow and temperature fields. These observations serve towards further validating our model and verifying the results. In Subsections 3.4-3.6, we develop an analytical close form for a correlation, suggest a set of correlations and compare our correlations with the literature. Finally, in Subsections 3.7-3.13, we report our results for the inclined heat sink case.

### *3.1 Heat sink length dependence*

On all surfaces of the hot vertical plate-fin heat sink, boundary layers develop starting from the bottom, as in the case of natural convection from a vertical flat plate. Boundary layer thicknesses increase throughout the length of the heat sink. Therefore, the average heat transfer coefficient depends on the heat sink length. Shorter lengths give rise to higher heat transfer coefficients due to lower boundary layer thicknesses. However, increasing the length also increases the heat transfer area hence the convective heat transfer rate. In Fig. 4, in order to observe the heat sink length dependence, the heat convection rates per unit base area versus the fin spacing are plotted for two different lengths of heat sinks of 15 mm fin height. Here, the heater input power is taken as 75 W.

The length of 250 mm corresponds to higher convective heat transfer rates per unit base area. The same effect is observed for the remaining four heater input powers.

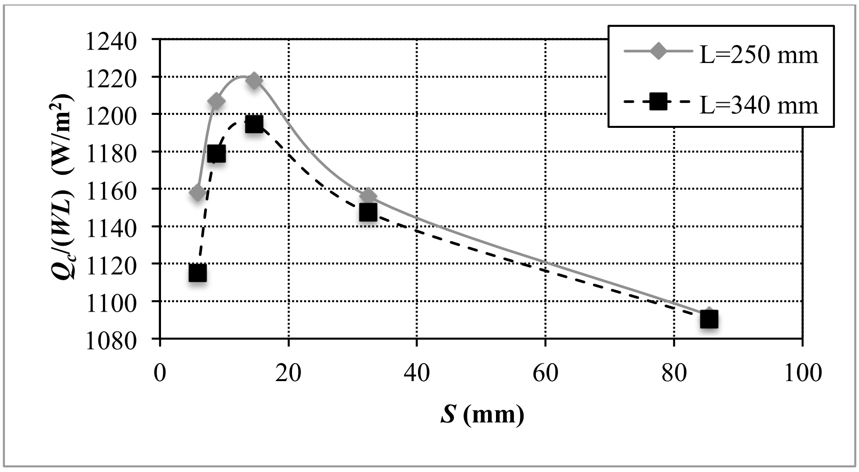


Fig. 4. Length dependence. Comparison of convective heat transfer rates per unit base area for two heat sink lengths for the heater input power of 75 W and for the fin height of 15 mm.

*3.2 Fin height dependence*

As the fin height increases, interaction between each fin surface boundary layer and the base surface boundary layer changes. Moreover, inlet of fresh air from the ambient to the heat sink channels along the length changes with the fin height. To show this effect, a shorter heat sink of 100 mm length with 14.7 mm fin spacing is simulated with heater input power of 25 W. The velocity vectors for $H$= 5, 15 and 25 mm are presented in Fig. 5. As the fin height increases, it is observed that distinguishably more air enters from the open side of the heat sink throughout its length. For $H$=25 mm, air entrance continues all the way to the top of the heat sink, whereas for $H$=5 mm, entrance of air is limited to the very bottom part of the heat sink.

The differences in flow structure directly affect the convective heat transfer from the heat sinks. When the fin height is increased while keeping all the other parameters constant, the convective heat transfer rate increases due to the increased extended surface area. The cross-sectional temperature contours (on the $x$-$z$ plane) for all of the three fin heights are shown in Fig. 6. Here, $L$= 250 mm, $S$= 14.7 mm and $Q_{in}$= 50 W are kept constant. All three sub-figures have the same temperature scale. The heat sink with $H$=25 mm transferred more heat, as a result, has a significantly lower (about 30 °C) temperature. Fig. 6 also confirms that keeping the fin thickness at 3 mm and the base thickness at 5 mm are good choices for obtaining a uniform temperature distribution in the heat sink. For all three values of $H$, the heat sink temperature is uniform, both through the height of the fins and the width of the heat sink base.

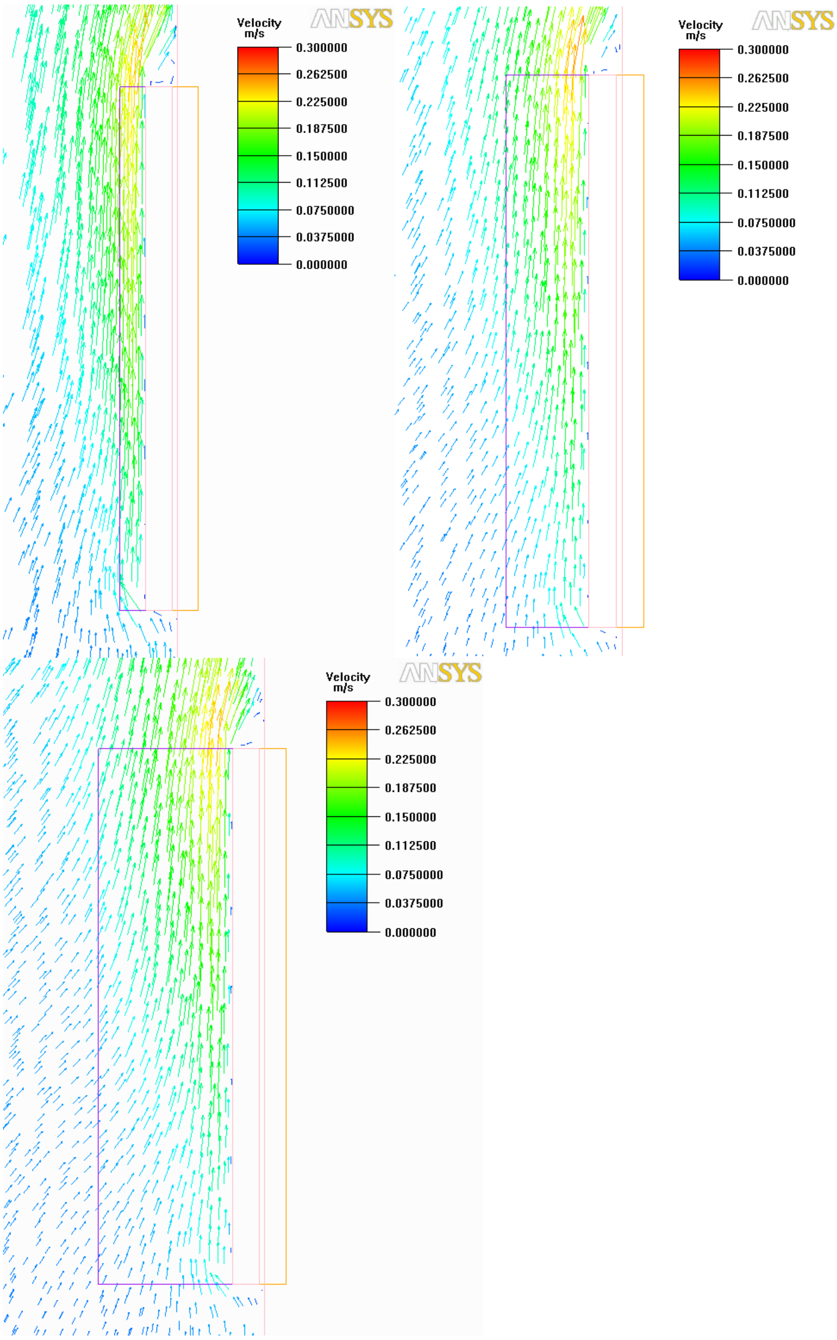


Fig. 5. Fin height dependence. Speed vectors for 3 different fin heights, $H$=5 mm (top left), 15 mm (top right) and 25 mm (bottom).

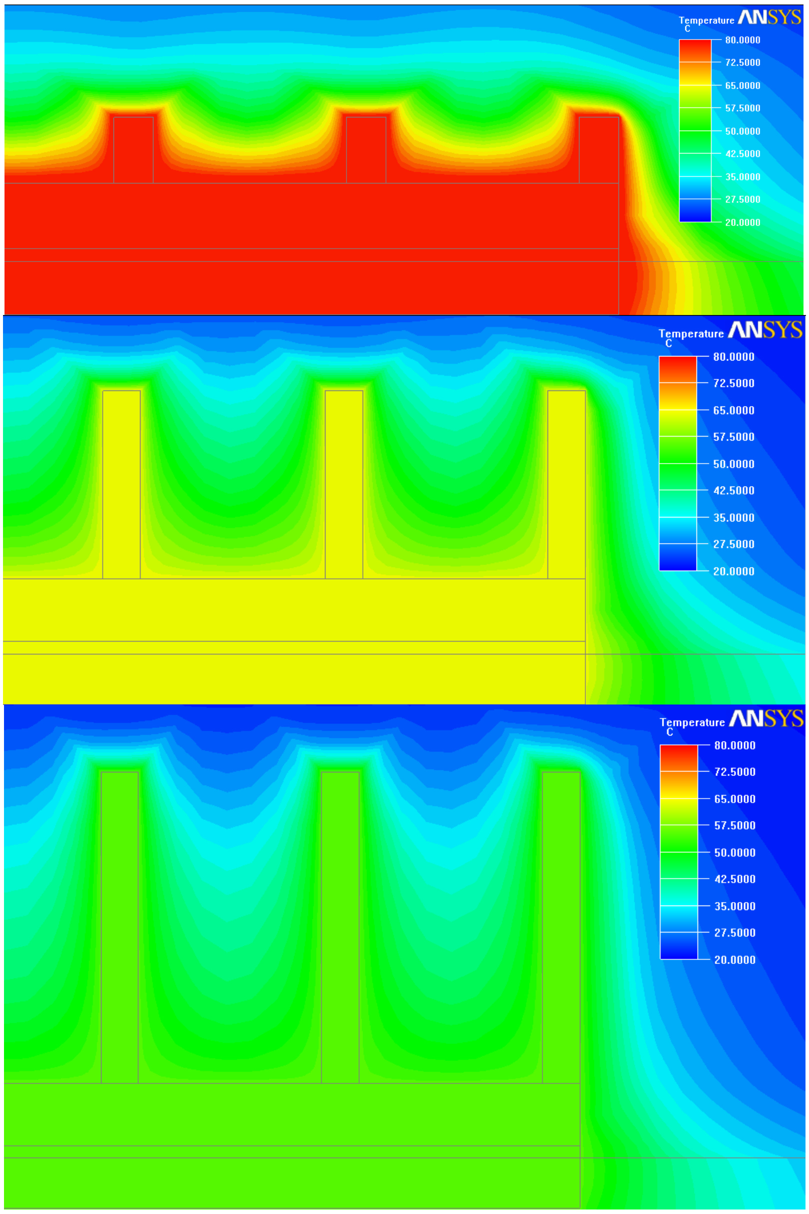


Fig. 6. Temperature distributions for 3 different fin heights with the same temperature scale, $H$=5 mm (top), 15 mm (middle) and 25 mm (bottom) for $L$= 250 mm, $S$= 14.7 mm and $Q_{in}$= 50 W.

In Fig. 7, heat convection rates per unit base area versus the fin spacing for three different fin heights are plotted for $L$=250 mm and $Q_{in}$=75 W. The following observations are made: Firstly, 5 mm fins are not very effective. Secondly, going from 15 mm to 25 mm fin height does not give as much improvement as going from 5 mm to 15 mm. Finally, for 5 mm fin height, the effect of fin spacing on convective heat transfer rate is very weak.

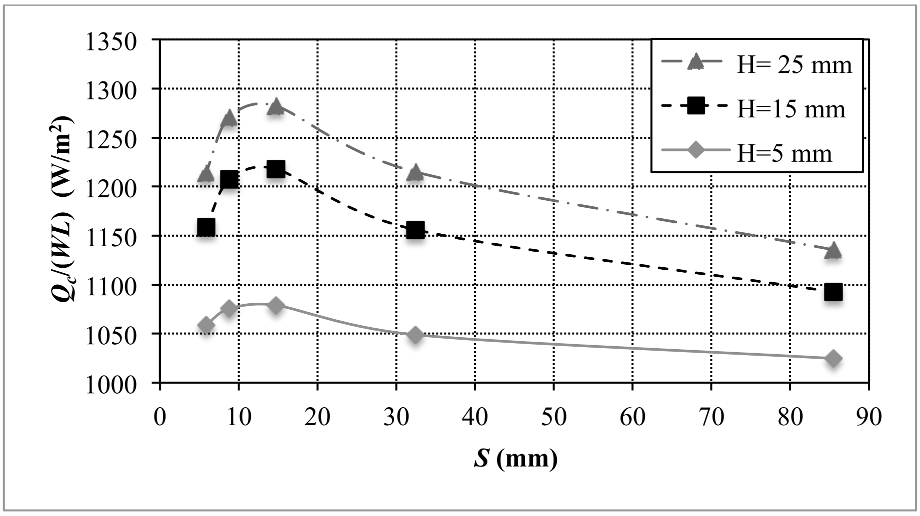


Fig. 7. Comparison of convective heat transfer rates per unit base area for three heat sink heights for the heater input power of 75 W and heat sink length of 250 mm. Optimum fin spacing is around 12 mm.

### *3.3 Optimum fin spacing*

As depicted in Figs 4 and 7, with increasing fin spacing, heat convection rate as a function of fin spacing at first increases up to a maximum value, and then decreases monotonically, when the heater input power is fixed at 75 W. Similar behavior is also observed when the heater power is fixed at any of the four remaining values. Moreover, for all five input powers, the optimum fin spacing is around 12 mm.

In experimental studies, investigators are limited with their experimental set up. In contrast, in CFD simulations, one can easily vary geometric parameters. To determine the optimum fin spacing, six different fin spacing values around 12 mm are tried and the optimum value is determined by following the procedure that was explained in Section 2.3.

The pair of plots in Fig. 8 respectively depict the wall temperature and the convective heat transfer rate as a function of fin spacing; in both cases, $L$=250 mm and $Q_{in}$=25 W. In order to find the optimum fin spacing values, a polynomial curve is fitted to each data set. By differentiating the polynomials, the specific fin spacing values at which either the convection heat transfer is at maximum or the wall temperature at minimum can be found. The optimum fin spacing values maximizing the convective heat transfer rate and minimizing the wall temperature are presented respectively in Tables 5 and 6. The differences between the two tables are due to changing view factors with fin spacing and related changes in radiation heat losses. Since minimizing the wall temperature includes the changes in radiative transfer, it may be a better approach. For comparison, the optimum fin spacing values obtained in [14] are tabulated in Table 7 (note that the first column data is $\Delta T$, instead of $Q_{in}$). Table 7 results were obtained for the heat sinks having $S$ values of 5.85, 8.8, 14.7, 32.4 and 85.5 mm while the $S$ values for Table 6 results are 8.8, 9.6, 10.6, 11.8, 13.1 and 14.7 mm. Therefore, when the agreement is not very good, considering that the optimum is around 12 mm, our Table 6 results should be trusted.

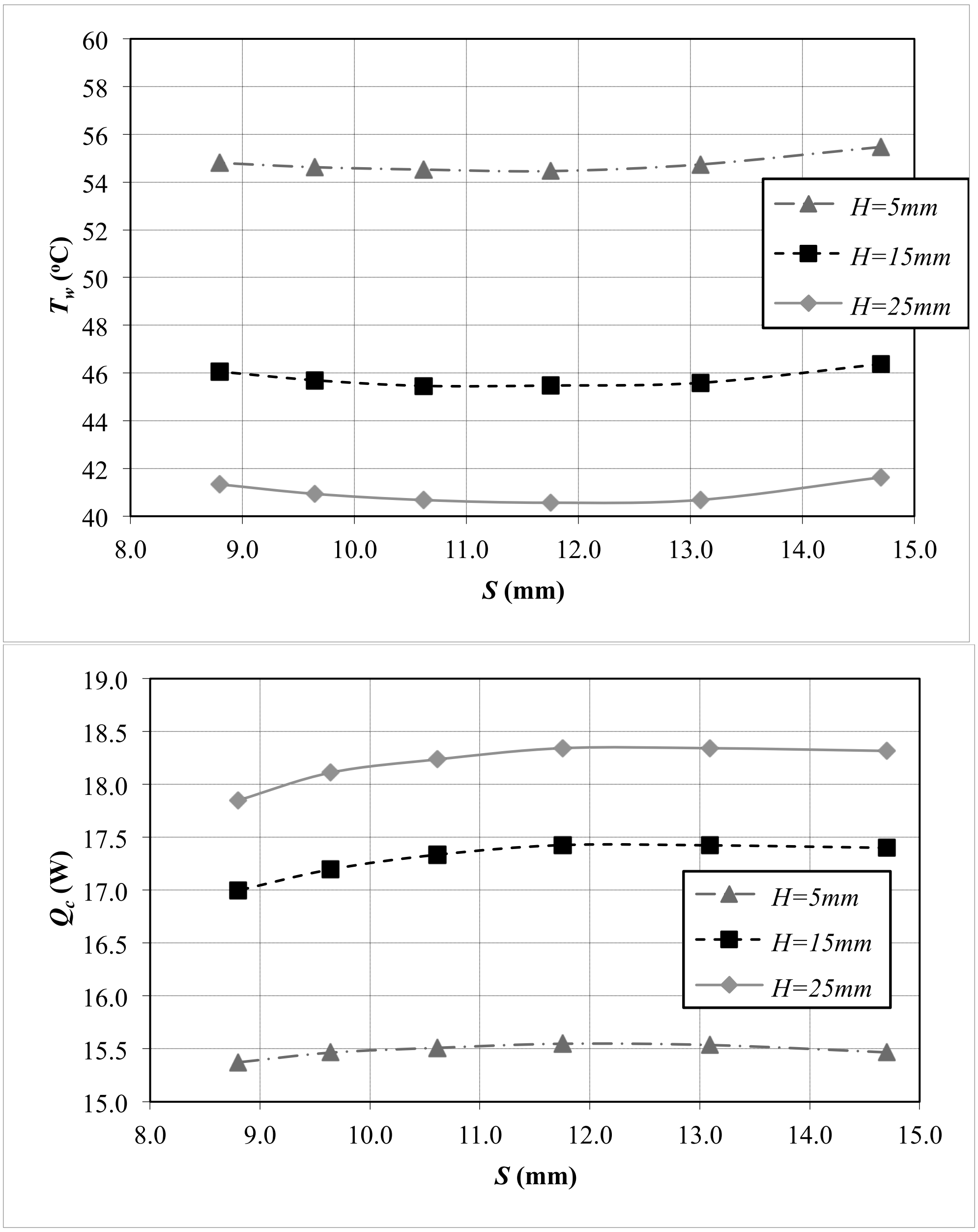


Fig. 8. Determining optimum fin spacing: minimizing wall temperature (top) and maximizing convective heat transfer rate (bottom). Examples are for $L$=250 mm and $Q_{in}$=25 W.

Table 5 Optimum fin spacing values for maximizing convection heat transfer rate

| $Q_{in}$ (W) | Optimum Fin Spacing, $S_{opt}$ (mm) | | | | | |
|---|---|---|---|---|---|---|
| | $L$=250 mm | | | $L$=340 mm | | |
| | $H$=25 mm | $H$=15 mm | $H$=5 mm | $H$=25 mm | $H$=15 mm | $H$=5 mm |
| 25 | 12.6 | 12.5 | 12.2 | 12.7 | 12.6 | 12.5 |
| 75 | 12.5 | 12.3 | 11.8 | 12.4 | 12.3 | 12.1 |
| 125 | 12.1 | 11.9 | 11.7 | 12 | 12.1 | 11.9 |

Table 6 Optimum fin spacing values for minimizing average temperature

| $Q_{in}$ (W) | Optimum Fin Spacing, $S_{opt}$ (mm) | | | | | |
|---|---|---|---|---|---|---|
| | $L$=250 mm | | | $L$=340 mm | | |
| | $H$=25 mm | $H$=15 mm | $H$=5 mm | $H$=25 mm | $H$=15 mm | $H$=5 mm |
| 25 | 11.6 | 11.5 | 11.1 | 11.7 | 11.6 | 11.4 |
| 75 | 11.3 | 10.8 | 10.8 | 11.4 | 11.5 | 11 |
| 125 | 11.4 | 10.6 | 10.5 | 11.3 | 11.4 | 11 |

Table 7 Optimum fin spacing values from Ref. [14]

| $\Delta T$ (K) | Optimum Fin Spacing, $S_{opt}$ (mm) | | | | | |
|---|---|---|---|---|---|---|
| | $L$=250 mm | | | $L$=340 mm | | |
| | $H$=25 mm | $H$=15 mm | $H$=5 mm | $H$=25 mm | $H$=15 mm | $H$=5 mm |
| 50 | 11 | 10.9 | - | 11.9 | 11.8 | - |
| 75 | 10.9 | 10.8 | 10.7 | 11.8 | 11.7 | 11.6 |
| 100 | 10.8 | 10.7 | 10.6 | 11.7 | 11.6 | 11.5 |
| 125 | 10.7 | 10.6 | 10.5 | 11.6 | 11.4 | 11.4 |

### *3.4 Analytical derivation for a correlation*

Let us consider the buoyancy driven flow of air in the channel between two adjacent fins. The coordinate system is the same as the one used in the numerical model (Fig. 2). Flow velocity in $x$-direction (along the width of the heat sink, perpendicular to fin side surfaces) is $u$=0. The gravitational acceleration $g$ is in $y$-direction (along the length); flow velocity in $y$-direction is $v$. $z$-direction is along the fin height; flow velocity in $z$-direction is $w$. The governing equations can be written as the following:

*Continuity equation*

$$\frac{\partial v}{\partial y}+\frac{\partial w}{\partial z}=0 \tag{5}$$

*x-momentum equation*

$$\frac{\partial p}{\partial x}=0 \tag{6}$$

*y-momentum equation*

$$\rho v\frac{\partial v}{\partial y}+\rho w\frac{\partial v}{\partial z}=-\frac{dp}{dy}+\mu\left(\frac{\partial^2 v}{\partial x^2}+\frac{\partial^2 v}{\partial y^2}+\frac{\partial^2 v}{\partial z^2}\right)+\rho g\beta\Delta T \tag{7}$$

*z-momentum equation*

$$\rho v\frac{\partial w}{\partial y}+\rho w\frac{\partial w}{\partial z}=-\frac{dp}{dz}+\mu\left(\frac{\partial^2 w}{\partial x^2}+\frac{\partial^2 w}{\partial y^2}+\frac{\partial^2 w}{\partial z^2}\right) \tag{8}$$

*Energy equation*

$$\rho c_p v\frac{\partial T}{\partial y}+\rho c_p w\frac{\partial T}{\partial z}=\left(v\frac{dp}{dy}+w\frac{dp}{dz}\right)+k\left(\frac{\partial^2 w}{\partial x^2}+\frac{\partial^2 w}{\partial y^2}+\frac{\partial^2 w}{\partial z^2}\right) \tag{9}$$

In order to obtain a form for dimensionless correlation, we need to non-dimensionalize Eqs (5)-(9). The non-dimensional coordinates are (*X, Y, Z*)

$$X=\frac{x}{S}\qquad Y=\frac{y}{L}\qquad Z=\frac{z}{H} \tag{10}$$

The non-dimensional velocity components are given as

$$\mathcal{V} = \frac{v}{v'} \qquad \mathcal{W} = \frac{w}{w'} \tag{11}$$

The characteristic velocity in the $y$-direction is proportional to the body force $\rho g$, the volumetric expansion coefficient $\beta$, the temperature excess $(T - T_a)$ of air between two adjacent fins and the ambient air, the channel cross sectional area in $y$-direction $SH$, and inversely proportional to dynamic viscosity $\mu$. To non-dimensionalize $y$-direction velocity, let us define

$$v' = \frac{\rho g \beta (T_w - T_a) SH}{\mu} \tag{12}$$

To satisfy the continuity equation in non-dimensional form

$$\frac{v' \partial \mathcal{V}}{L \partial Y} = -\frac{w' \partial \mathcal{W}}{H \partial Z} \quad \textit{i.e.} \quad \frac{v'}{L} = \frac{w'}{H} \quad \text{thus} \quad w' = \left(\frac{H}{L}\right) v' \tag{13}$$

Non-dimensional temperature is defined as

$$\phi = \frac{T - T_a}{T_w - T_a} \tag{14}$$

Non-dimensional pressure is defined as

$$P = \frac{p}{\rho (v')^2} \tag{15}$$

After putting these definitions in Eqs (5)-(9), we obtain the non-dimensional form of the governing equations as the following:

*Continuity equation*

$$\frac{\partial \mathcal{V}}{\partial Y} + \frac{\partial \mathcal{W}}{\partial Z} = 0 \tag{16}$$

*x-momentum equation*

$$\frac{\partial P}{\partial X} = 0 \tag{17}$$

*y-momentum equation*

$$\mathcal{V} \frac{\partial \mathcal{V}}{\partial Y} + \mathcal{W} \frac{\partial \mathcal{V}}{\partial Z} = -\frac{dP}{dY} + \frac{\nu}{Hw'} \left[ \left(\frac{H}{S}\right)^2 \frac{\partial^2 \mathcal{V}}{\partial X^2} + \frac{\partial^2 \mathcal{V}}{\partial Y^2} + \left(\frac{H}{L}\right)^2 \frac{\partial^2 \mathcal{V}}{\partial Z^2} \right] + \frac{\nu}{v' S} \tag{18}$$

*z-momentum equation*

$$\mathcal{V} \frac{\partial \mathcal{W}}{\partial Y} + \mathcal{W} \frac{\partial \mathcal{W}}{\partial Z} = -\left(\frac{L}{H}\right)^2 \frac{dP}{dZ} + \frac{\nu}{Hw'} \left[ \left(\frac{H}{S}\right)^2 \frac{\partial^2 \mathcal{W}}{\partial X^2} + \frac{\partial^2 \mathcal{W}}{\partial Y^2} + \left(\frac{H}{L}\right)^2 \frac{\partial^2 \mathcal{W}}{\partial Z^2} \right] \tag{19}$$

*Energy equation*

$$\begin{aligned} \frac{\nu}{Sw'} \left( \mathcal{V} \frac{\partial \phi}{\partial Y} + \mathcal{W} \frac{\partial \phi}{\partial Z} \right) &= \frac{g \beta L}{c_p} \left( \mathcal{V} \frac{dP}{dY} + \mathcal{W} \frac{dP}{dZ} \right) \\ &\quad + \frac{\nu k}{\rho c_p S H w'^2} \left[ \left(\frac{H}{S}\right)^2 \frac{\partial^2 \phi}{\partial X^2} + \frac{\partial^2 \phi}{\partial Y^2} + \left(\frac{H}{L}\right)^2 \frac{\partial^2 \phi}{\partial Z^2} \right] \end{aligned} \tag{20}$$

We obtain dimensionless groups by rearranging the groups in Eqs (18)-(20) as

$$\frac{\nu}{Hw'} = \left(\frac{\nu}{Sw'}\right) \left(\frac{S}{H}\right) \tag{21}$$

$$\frac{\nu}{Sw'} = \frac{\nu}{S \left[ \frac{g \beta (T_w - T_a) SH}{\nu} \right] \left(\frac{H}{L}\right)} = \frac{1}{\left[ \frac{g \beta (T_w - T_a) S^3}{\nu^2} \right] \left(\frac{H}{S}\right) \left(\frac{H}{L}\right)} \tag{22}$$

$$\frac{\nu k}{\rho c_p S H w'^2} = \frac{1}{\left(\frac{Sw'}{\nu}\right)^2 \left(\frac{H}{S}\right)\left(\frac{\mu c_p}{k}\right)} \tag{23}$$

The dimensionless groups are the following:
$\Pi_1 = H/L$, $\Pi_2 = S/H$, $\Pi_3 = [g\beta(T_w - T_a)S^3]/\nu^2 \equiv Gr$, $\Pi_4 = (\mu c_p)/k \equiv Pr$ and $\Pi_5 = g\beta L/c_p$. The first term on the right-hand-side of Eq. (20) is not important for small temperature differences (no significant pressure gradient in either direction) therefore $\Pi_5$ is negligible. By combining $\Pi_1$, $\Pi_2$ and $\Pi_3$ we can define a modified Grashof number:

$$Gr' = Gr(H/L)^{m_1}(S/H)^{m_2} \tag{24}$$

For a similar modification, the powers are previously suggested in [10] as $m_1 = 1/2$ and $m_2 = 1$, thus,

$$\begin{aligned} Gr' &= \{[g\beta(T_w - T_a)S^3]/\nu^2\}(S/H)(H/L)^{1/2} \\ &= [g\beta(T_w - T_a)S^4]/[\nu^2(HL)^{1/2}] \end{aligned} \tag{25}$$

The average Nusselt number based on *S* should be a function of $Gr'$ and $Pr$; it takes the simple form:

$$\overline{Nu_S} \equiv \frac{hS}{k} = C(Gr'Pr)^n \tag{26}$$

Leung and Probert [10] obtained a similar relation in which they had an exponential fin effectiveness term that we do not need due to the high thermal conductivity of aluminum. They used

$$n = \begin{cases} 1/2 \ \text{ for } Gr'Pr < 250 \\ 1/3 \ \text{ for } 250 < Gr'Pr < 10^6 \end{cases} \tag{27}$$

*3.5 Average Nusselt number correlation*

Using the form, Eq. (26), we process our entire data in the two respective ranges in Eq. (27). Based on power curve fits (Fig. 9), we obtained *C* constant coefficients of 0.0929 and 0.2413 which are the mid points of the respective 95% confidence intervals of 0.0929±0.0016 and 0.2413±0.0016, in $Gr'Pr < 250$ and $250 < Gr'Pr < 10^6$ ranges, respectively. The squared correlation coefficients ($R^2$) of the fits are 0.9607 and 0.9932 for the first and second ranges, respectively, that is, the suggested form fits very well to our data. Thus, we suggest the following correlations:

$$\boxed{\begin{aligned} \overline{Nu_S} &= 0.0929(Gr'Pr)^{0.5} \quad \text{for } Gr'Pr < 250 \\ \overline{Nu_S} &= 0.2413(Gr'Pr)^{1/3} \quad \text{for } 250 < Gr'Pr < 10^6 \end{aligned}} \tag{28}$$

In addition to the two ranges in Eq. (28), we have a third range of data points where $Gr'Pr > 10^6$ (marked with triangles in Fig. 9). The data in this final region corresponds to a fin spacing of 85.5 mm. Because the fin spacing is very large, the fins act like individual plates. As a result, their height and length become important. Observe that the data appears to be both fin height and length dependent. Note, however, that configurations with small numbers of fins, hence, large fin spacing values may not be practical choices; thus, we do not suggest any correlation for that region.

In the same figure (Fig. 9), the entire data that is clustered in $10^4$-$10^6$ range of $Gr'Pr$ is obtained for the fin spacing of 32.4 mm. Again, due to this large fin spacing, the fins continue to act like individual plates; thus, the height and length dependence of $Nu_S$ does still exist. The practical choices of fin spacing are expected to fall in $Gr'Pr < 10^4$ range.

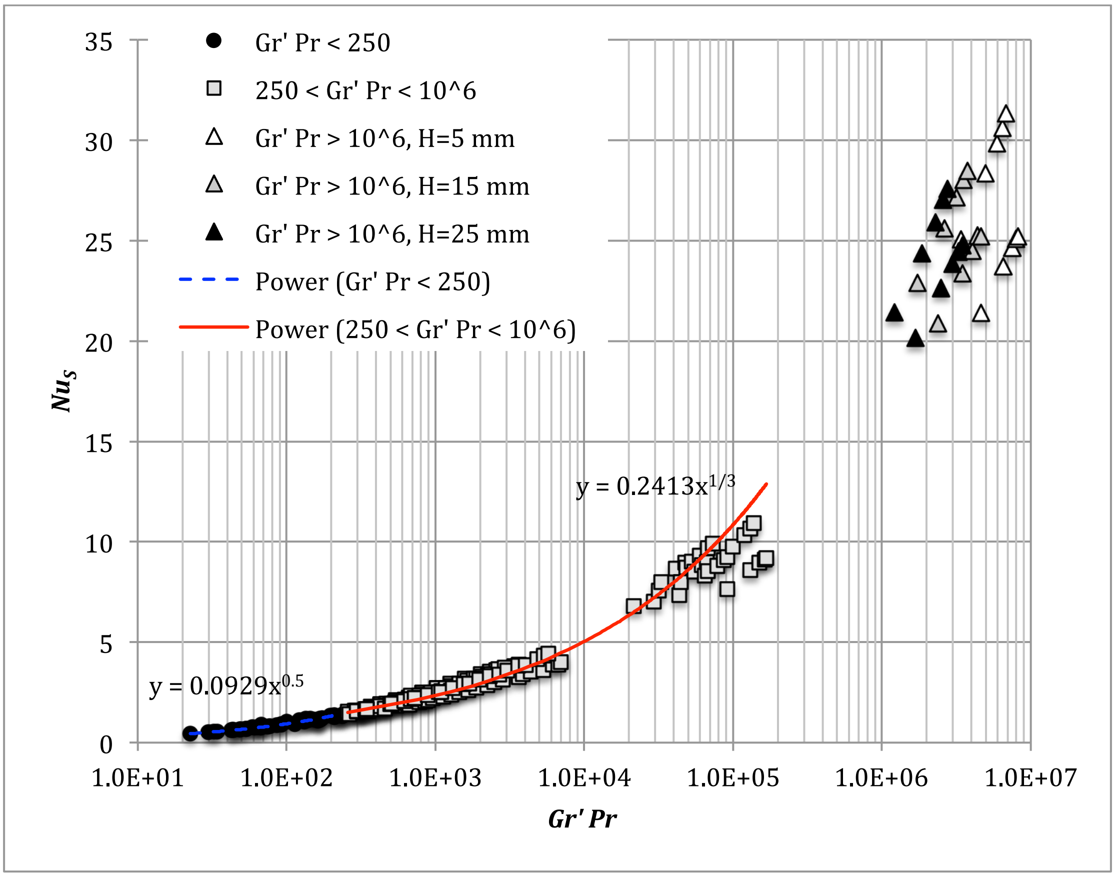


Fig. 9. Analysis of entire data for the power function fits in the form of Eq. (26).

In Fig. 10, the data restricted to $250 < Gr'Pr < 10^4$ range is further analyzed. It is observed that the fins of $H$=5 mm show heat sink length dependence; all of the points (marked with •) above the dashed line are for $L$= 250 mm, while the ones on the other side are for $L$= 340 mm. This very small fin height is not practically very useful. (Nevertheless, a correlation where $C$=0.2301 and $n$=1/3 can be obtained). In contrast, $H$=15 and 25 mm data in the same $Gr'Pr$ range (marked with □) does not show dependence to either the fin height or the length. Additionally, this fin height range is very practical for engineering applications. Therefore, it may worth considering the range $250 < Gr'Pr < 10^4, H \geq 15\ mm$ separately. Fitting power curve to the data in this range, $C$=0.252 is obtained as the mid point of the 95% confidence interval 0.2520±0.0026. The squared correlation coefficient $R^2$ is 0.9705. Notice that $C$ value here is higher than the $C$ value in Eq. (28b).

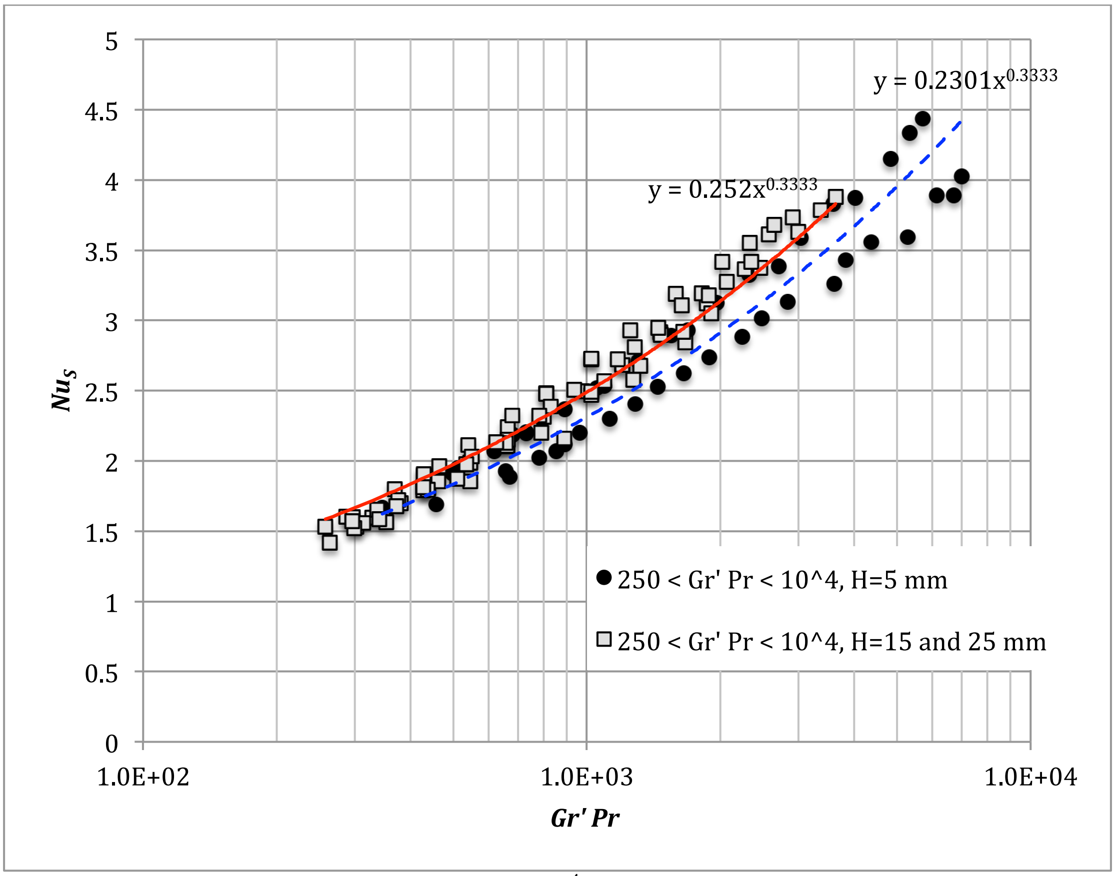


Fig. 10. Analysis of data in $250 < Gr'Pr < 10^4$ range. The results for $H$= 5 mm (marked with •) depends on $L$; all of the points above the dashed line are for $L$= 250 mm, while the ones on the other side are for $L$= 340 mm. No $L$ dependence is observed for $H$= 15 and 25 mm.

Interestingly, for the data obtained for the heat sinks with $S$=$S_{opt}$=11.75 mm and H=15 and 25 mm, the constant coefficient $C$ is determined to be 0.2543, with the 95% confidence interval of 0.2543±0.0056; $R^2$ is 0.9295. That is, also around $S_{opt}$, $C$ value is higher than the $C$ value in Eq. (28b).

As a result, for the smaller range of $Gr'Pr$, we recommend the following alternative:

$$\boxed{\overline{Nu_S} = 0.252(Gr'Pr)^{1/3} \quad \text{for } 250 < Gr'Pr < 10^4, H \geq 15\ mm} \tag{29}$$

*3.6 Comparison with experimental literature*

A good way to judge the accuracy of a suggested correlation is to compare Nusselt numbers calculated directly from the model parameters and the data with those calculated from the correlation. In Figs 11-13, we provide several parity plots comparing our correlation with the previous vertical correlations due to Elenbaas [5] and Leung and Probert [10]. In each figure, there are 3 parity plots, corresponding to the two previously suggested ones and ours. The $x$-axis values depict direct results whereas the $y$-axis values depict the results from the respective correlations. For each of the three parity plots to be compared, we also draw their best fitting line to give an idea of the overall trend for each correlation. An ideal correlation is expected to lie along the diagonal ($y$=$x$), called *parity line.* To rule out the effect of the choice of data, we repeat the procedure using two more data sets, in Figs 12 and 13. The data set used in Fig. 12 is due to Leung *et al.* [7,8,9] and the one in Fig. 13 is due to Starner and McManus [2].

For the first data set (Fig. 11) our correlation is almost on the parity line, the diagonal. Elenbaas [5] correlation is also quite good, with its trend line deviating slightly from the parity line. The trend line for the Leung and Probert [10] correlation, on the other hand, significantly deviates from the parity line. Note that the considered data fall within the range of all three correlations $250 < Gr'Pr < 10^4$. When the procedure is repeated for Leung *et al.* data [7,8,9], trend lines for the parity plots of all three correlations deviate from the parity line almost the same amount (Fig. 12). Whereas Leung and Probert correlation overestimates, both our correlation and Elenbaas one underestimate.

When the procedure is repeated for Starner and McManus [2] data, which falls in $Gr'Pr < 250$, the trend line of the parity plot for our correlation (Eq. (28a)) is almost on the parity line (Fig. 13). Whereas Elenbaas correlation underestimates, Leung and Probert one overestimates.

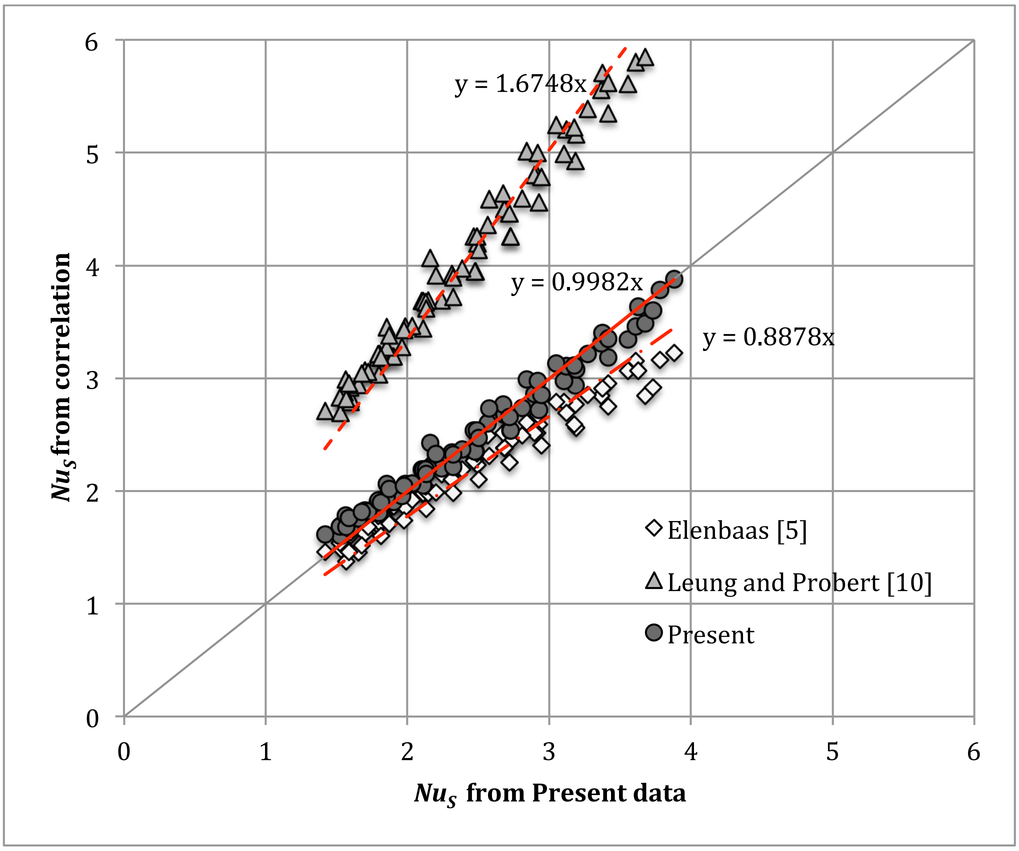


Fig. 11. Comparison of $Nu_S$ parity plots using present data for present Eq. (29), Elenbaas [5] correlation, and Leung and Probert [10] correlation.

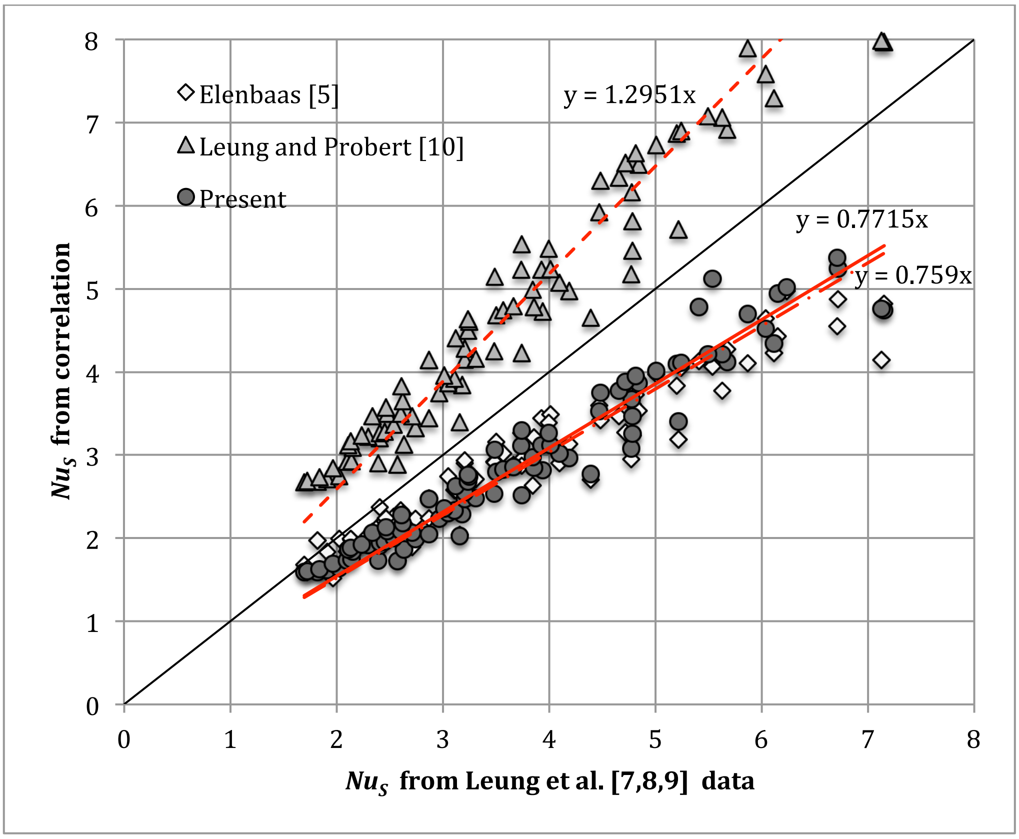


Fig. 12. Comparison of $Nu_S$ parity plots for present Eq. (29), Elenbaas [5] correlation, and Leung and Probert [10] correlation. Data from Leung *et al.* [7,8,9] is used.

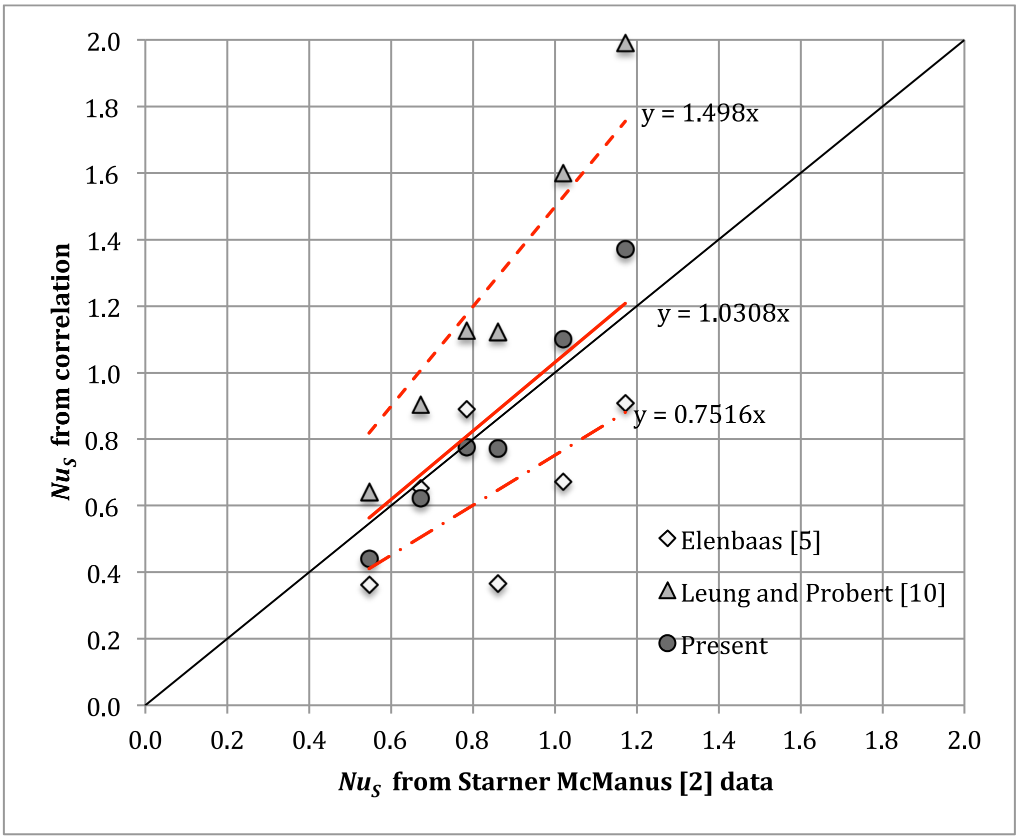


Fig. 13. Comparison of $Nu_S$ parity plots for present Eq. (27), Elenbaas [5] correlation, and Leung and Probert [10] correlation. Data from Starner and McManus [2] is used.

### *3.7 Upward inclination flow structure*

When a hot plate-fin heat sink is inclined from the vertical in upward facing orientation, since the wall temperature is higher than the ambient air temperature, cooler air entering from the bottom side or (at inclinations close to horizontal) from both the top and bottom sides of the heat sink heats up. Consequently, a plume of air rises from the heat sink at a location that depends on the inclination angle. Note that there is also cool air entrance along the heat sink from the open side of the channel formed by the consecutive fins. Since the driving force behind the phenomenon is the buoyancy force, regardless of the inclination angle, a plume rises in the opposite direction of the gravitational acceleration, as can be seen in Fig. 14 depicting fluid temperature contours at the inclination angles of -45°, -75° and -90° for the heater power of 75 W and fin height of 25 mm. The heat sink fin is shown as a wireframe in order to make fluid velocity in the channel between two adjacent fins visible. The heat sink base is also visible due to its higher temperature. When the subfigures are compared, it is observed that the base temperature increases with the increasing angle, indicating lower heat transfer rates at higher angles. At -45°, the plume is at the top end of the heat sink (Fig 14a); at -75°, it rises from a location on the heat sink; and at upward horizontal (-90°), it is at the center of the heat sink.

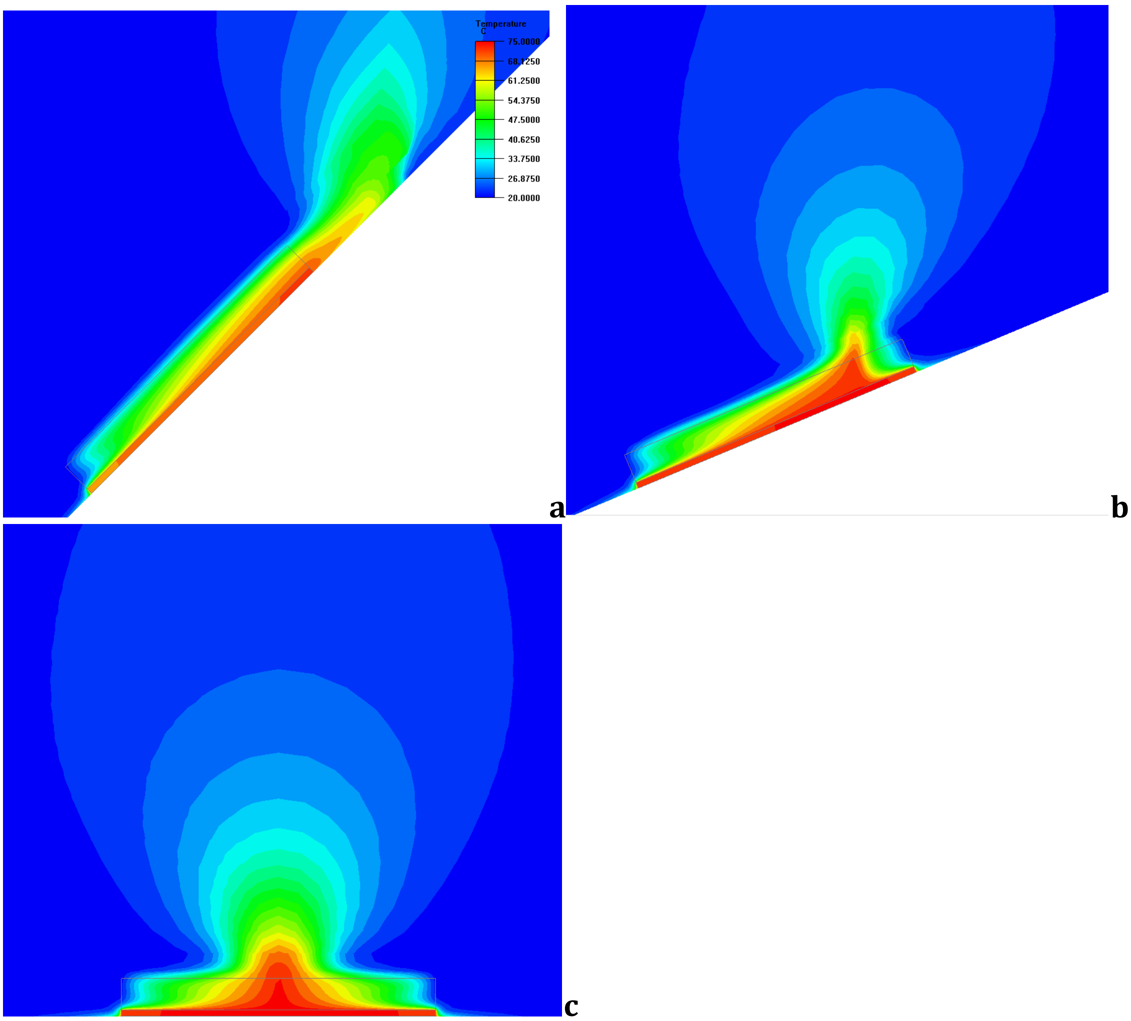


Fig. 14. Temperature contours for upward inclined heat sink at -45°, -75° and -90° (from top to bottom) for $Q_{in}$=75 W and $H$=25 mm (side views of the heat sink).

At each inclination angle, the density of the fluid changes with the fluid temperature. As a result, different buoyancy driven flow structures are formed. Such flow structures at the inclination angles of 0°, -45°, -60°, -75°, -85° and -90° for $Q_{in}$=75 W, $H$=25 mm are shown in Fig. 15. All of the subfigures have the same scale, which is shown in Fig. 15a.

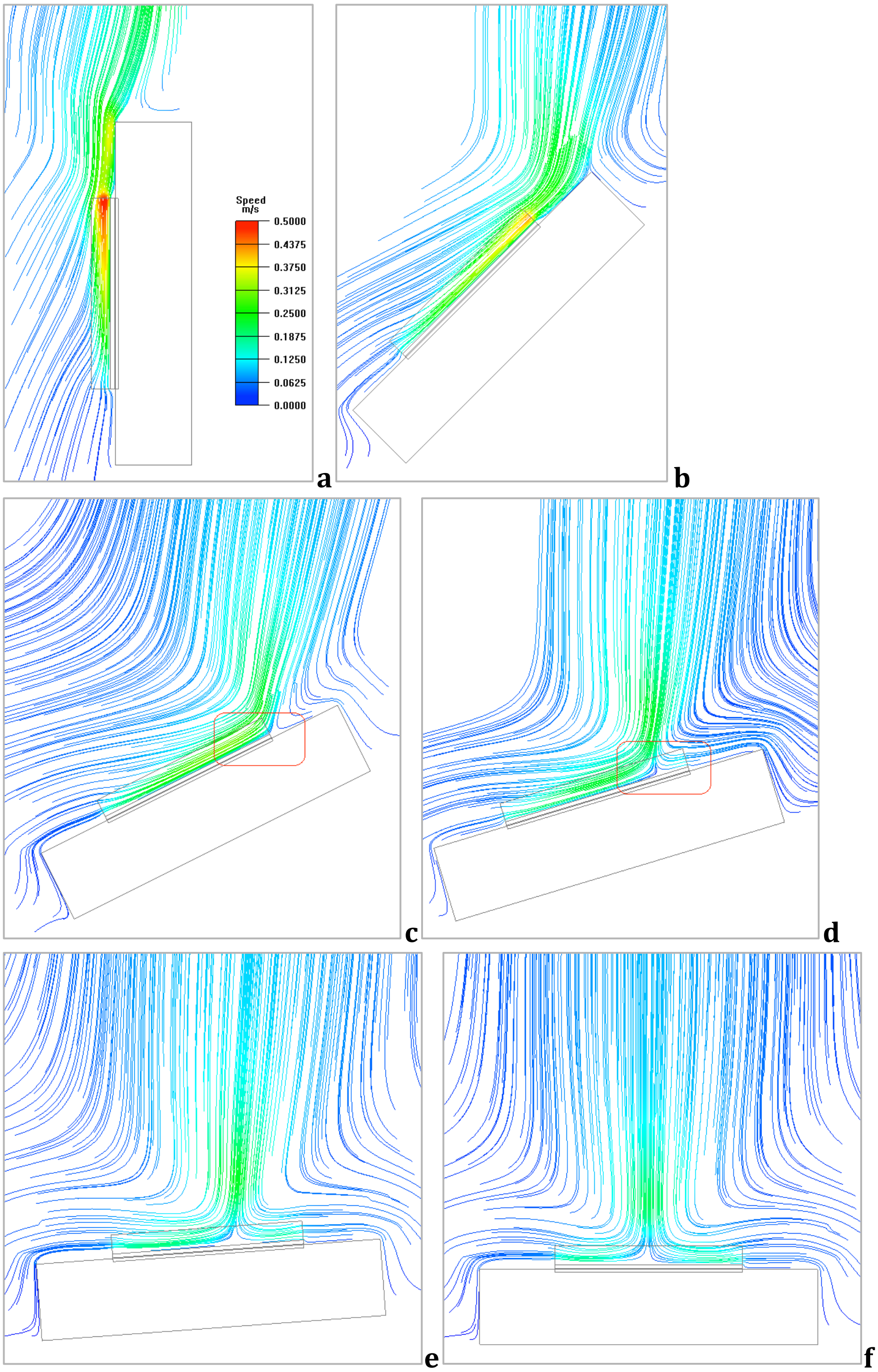


Fig. 15. Streamlines for a) the vertical (0°) and *upward inclined* heat sinks at b) -45°, c) -60°, d) -75°, e)-85° and f) -90° for $Q_{in}$=75 W and $H$=25 mm (side views of the heat sink and insulation). Flow separation locations are marked with red rectangles.

As inclination increases, flow velocities at the exit (top end) of the heat sink reduce. As apparent from the figures, *e.g.*, from Fig. 15a to 15b, the color changes from red to orange. In Figs 15c and 15d, flow separation locations are marked with red rectangles. It is observed that for the upward case the separation location starts to move from the tip towards the center after -60° of inclination. At -90°, the flow is symmetric around the center of the heat sink, placing the separation location to the center.

### *3.8 Downward inclination flow structure*

When a hot plate-fin heat sink is inclined from the vertical in downward direction, since the wall temperature is higher than the ambient air temperature, cooler air entering into the channel between two consecutive fins heats up along the heat sink and then escapes from the top side or (at inclinations close to horizontal) from both the top and bottom sides of the heat sink. Such flow structures at the inclination angles of 0°, +45°, +60°, +75°, +80°, +85° and +90° for $Q_{in}$=75 W, $H$=25 mm are shown in Fig. 16.

In the downward horizontal orientation (+90°) (see Fig. 16g), air separates at the mid point of the heat sink length. As the inclination angle decreases, the separation point moves towards the leading edge of the heat sink (see the location for +85° in Fig. 16f marked with the rectangle). After reaching the leading edge, at around +80° (Fig. 16e), the separation point stays there for smaller inclination angles, hence, no separation along the heat sink is observed for $\theta < 80°$ (Figs 16a-d). These observations agree with the observations of Mittelman *et al.* [1].

The separation location and whether it is located on the heat sink or at the tip are important for the performance of the heat sink. We will revisit them in Section 3.12.

### *3.9 Inclination angle dependence of $T_w$, $Q_c$ and $Q_r$*

Variations of surface average temperature, convective heat transfer rate and radiative heat transfer rate with respect to inclination angle are shown for all of the three fin heights and $Q_{in}$=125 W in upward and downward inclinations in Figs 17 and 18, respectively.

From Fig. 17, we make the following observations for upward inclinations of the heat sink:

- Since the radiative heat transfer rate ($Q_r$) depends on the fourth power of the average heat sink temperature ($T_w$), both $Q_r$ and $T_w$ have similar dependence to the inclination angle.
- Starting from vertical up to -30°, the changes in $T_w$, $Q_c$ and $Q_r$ are very small; after -30°, $Q_c$ decreases until reaching a minimum.
- $T_w$, $Q_c$ and $Q_r$ at -85° are very close to the values at -90°.

From Fig. 18, we make the following observations for downward inclinations of the heat sink:

- $Q_c$ stays almost the same in 0-30° range, though at angles very close to vertical, it may be slightly larger than it is in the vertical case. This can be explained with the thinning of the boundary layer in small downward inclinations.
- $T_w$, $Q_c$ and $Q_r$ changes monotonically until the inclination gets very close to +90° (downward horizontal).
- $Q_c$ from downward horizontal heat sink is always significantly smaller than $Q_c$ from both vertical and upward horizontal heat sinks.

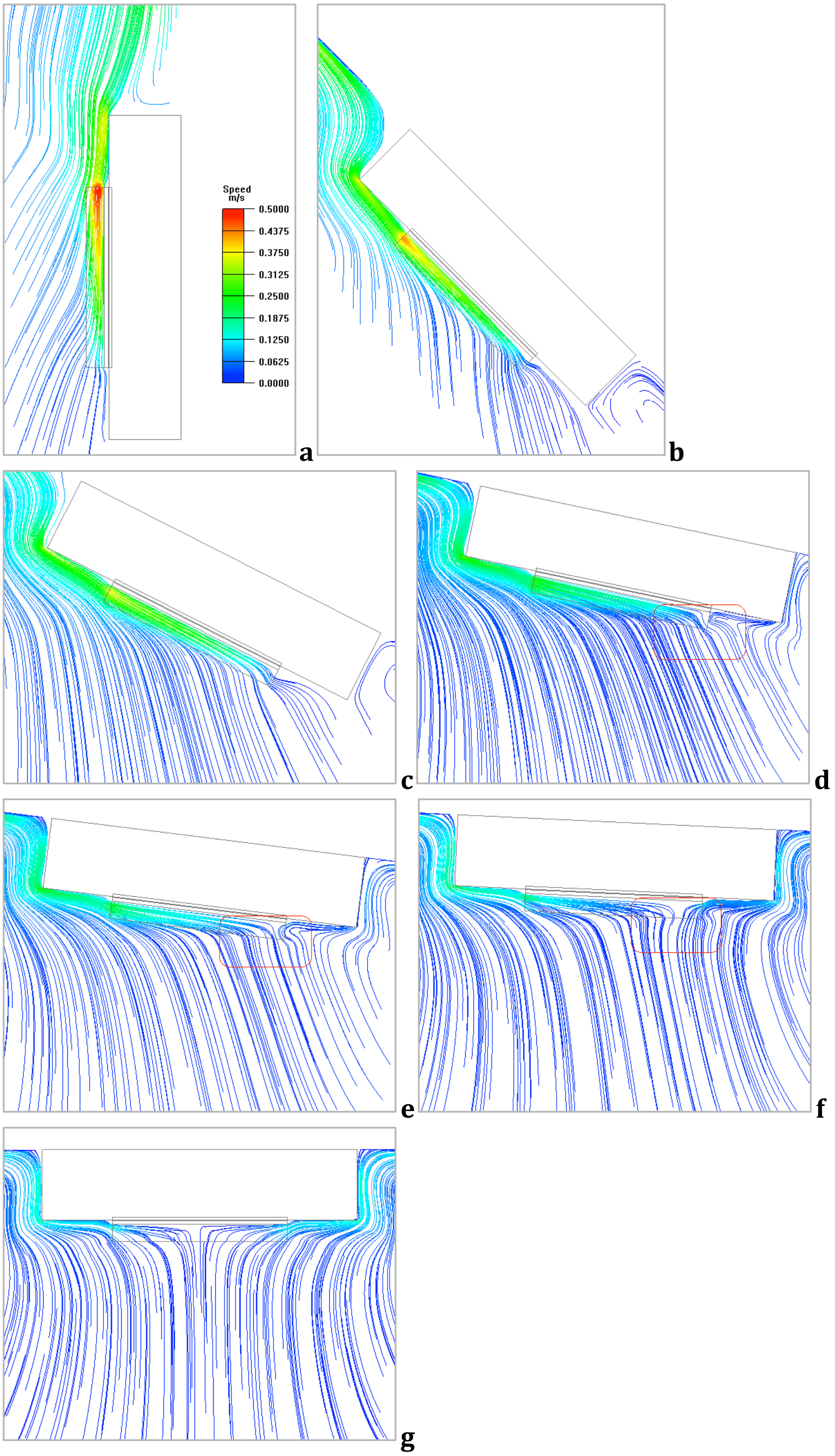


Fig. 16. Streamlines for a) the vertical and *downward inclined* heat sinks at b) 45°, c) 60°, d) 75°, e) 80°, f) 85° and g) 90° for $Q_{in}$=75 W and $H$=25 mm (side views of the heat sink and insulation). Flow separation locations are marked with red rectangles.

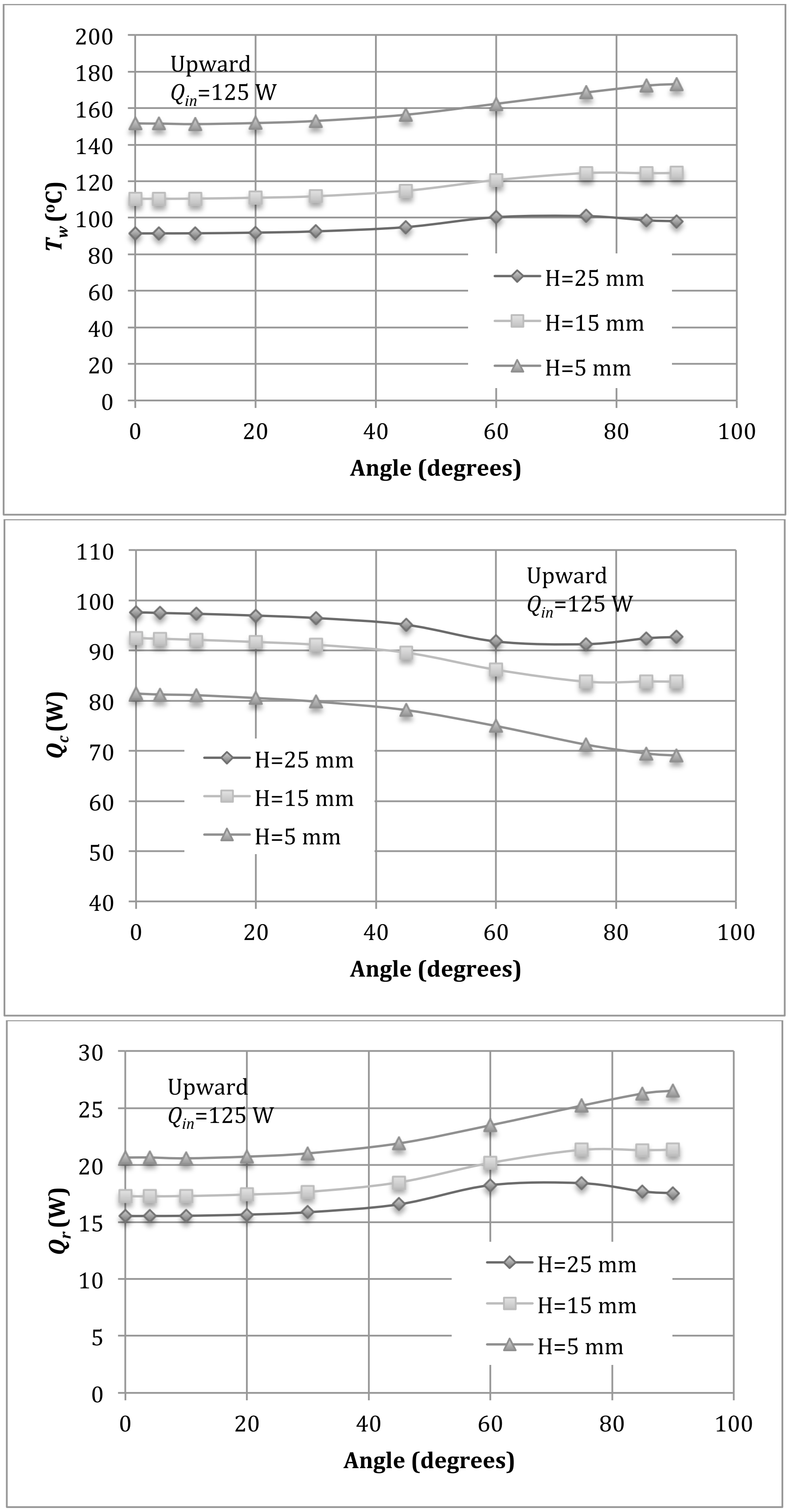


Fig. 17. Variations of surface average temperature (top), convective heat transfer rate (middle) and radiative heat transfer rate (bottom) with respect to inclination angle, for all of the three fin heights and $Q_{in}$=125 W in upward inclinations.

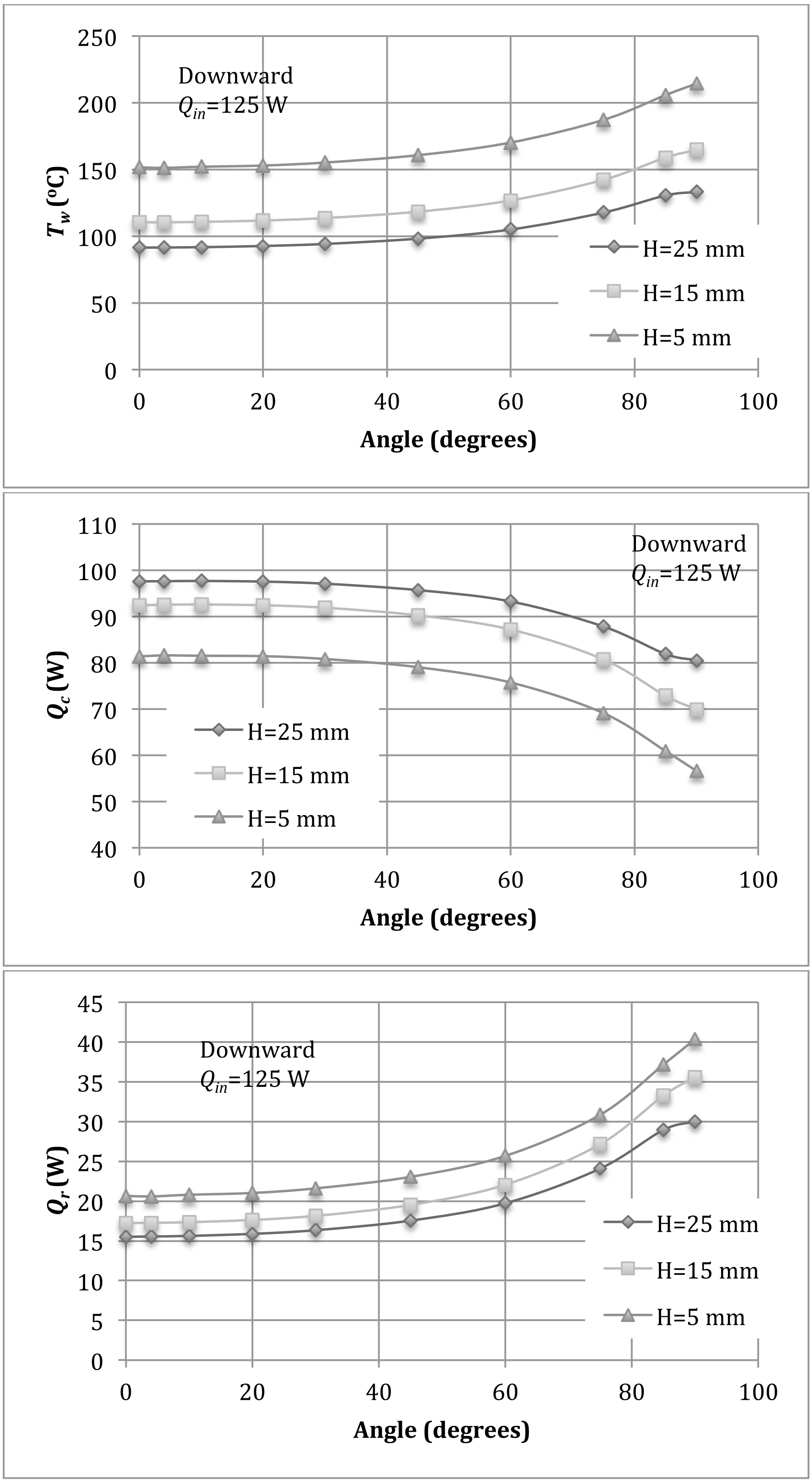


Fig. 18. Variations of surface average temperature (top), convective heat transfer rate (middle) and radiative heat transfer rate (bottom) with inclination angle for all of the three fin heights and $Q_{in}$=125 W in downward inclinations.

### *3.10 Fin height dependence*

Variation of convection heat transfer rate with fin height in upward inclination is shown for $Q_{in}$= 125 W in the middle sub-figure of Fig. 17.

From Fig. 17, we make the following fin height related observations for upward inclinations of the heat sink:

- With increasing $H$, the difference in $Q_c$ between vertical and upward horizontal heat sinks gets smaller.
- As the fin height increases, angle dependence of $T_w$, $Q_c$ and $Q_r$ decrease. This can be attributed to vertical plate like behavior of fins with large height protruding from the horizontal base.
- As the fin height increases, the gain from further increasing the fin height decreases.
- After -60°, the angle at which minimum of $Q_c$ is observed depends on the fin height ($H$).
- For $H$=5 mm, the minimum $Q_c$ is attained at -90° (upward horizontal). The angles at which a minimum is attained get smaller with increasing $H$.

Variation of the convection heat transfer rate with respect to the fin height in downward inclination for $Q_{in}$= 125 W is shown in the middle sub-figure of Fig. 18. The first three observations given above (based on Fig. 17) related to fin height dependence for upward inclinations are also valid for downward inclinations.

### *3.11 Validity range of modified vertical case correlations*

When a bare flat plate is inclined from the vertical, it has been observed that the correlations for vertical case are still valid up to 45° by only replacing $Ra$ with $Ra \cos\theta$ [26]. Behind this approach, there is an assumption that the flow structure stays the same, and the only change is in the body force, where the effective body force becomes $\rho g\cos\theta$. With the same rationale, the vertical case correlation for plate-fin heat sinks with the same modification is expected to be valid at small inclination angles, as long as the flow structure stays the same.

Modifying the correlations suggested in Section 3.5 for the vertical case by multiplying $Gr'$ with $\cos\theta$, we obtain

$$\boxed{\overline{Nu_S} = 0.0929(Gr'\,Pr\cos\theta)^{0.5} \quad \text{for } Gr'\,Pr\cos\theta < 250} \tag{30}$$

$$\boxed{\overline{Nu_S} = 0.2413(Gr'\,Pr\cos\theta)^{1/3} \quad \text{for } 250 < Gr'\,Pr\cos\theta < 10^6} \tag{31}$$

where $\overline{Nu_S} \equiv (hS)/k$ is the Nusselt number based on fin spacing $S$, $Pr$ is the Prandtl number, $Gr' = [g\beta\Delta TS^4]/[\nu^2(LH)^{0.5}]$ is the modified Grashof number, and $\theta$ is the inclination angle measured from the vertical.

Recall that in Eq. (29), an alternative correlation valid for $H$ = 15 and 25 mm in a narrower $Gr'Pr$ range covering all practical $S$ values has been suggested. Modifying it yields

$$\boxed{\overline{Nu_S} = 0.252(Gr'\,Pr\cos\theta)^{1/3} \quad \text{for } 250 < Gr'\,Pr\cos\theta < 10^4} \tag{32}$$

In Fig. 19, we compare the estimation of convection heat transfer rate obtained using the $\overline{Nu_S}$ correlation given by Eq. (32) to the rate given by simulation. Simulation data are marked with ×, the rates based on Eq. (32) with □. Both upward (top figure) and downward (bottom figure) inclinations are examined. Three different trends in each of the subfigures correspond to three different heater power values, *i.e.* 125, 75 and 25 W. Only $H$=15 and 25 mm cases are covered, as Eq. (32) is valid for these heights.

It is observed (top subfigure) that the two rates, *i.e.* simulated and estimated from correlation, agree very well for the upward inclination angles ranging 0-60°; for those larger than 60°, using Eq. (32) does not seem suitable. On the other hand, for the downward case (bottom subfigure), the rates agree in a wider inclination angle range of 0-80°. That is, Eq. (32) is observed to be valid from −60° to +80°.

Compared to the narrower range of similar correlations for bare flat plates, the surprisingly wide range of −60° to +80° may be attributed to the flow channels in between the consecutive fins, which are keeping the structure of the flow two dimensional for a very wide range of inclinations.

To better judge the validity of Eq. (32) in the above mentioned angle ranges, the best fitting power curves for the inclined data in the respective ranges are shown in Fig. 20. The estimated constant coefficients, which are respectively 0.2585 and 0.2538 for the upward and downward inclinations, are very close to 0.252, the coefficient of Eq. (32). This supports the validity of Eq. (32) in the respective ranges. The constant coefficients are the mid points of the respective 95% confidence intervals of 0.2585±0.0031 and 0.2538±0.0043. The squared correlation coefficients ($R^2$) of the fits are 0.9389 and 0.9484 for the upward and downward inclinations, respectively. Note that in Section 3.5 for the vertical case with $S$=$S_{opt}$=11.75 mm, we determined the constant coefficient as 0.2543±0.0056. Since both 0.2585 and 0.2538 fall within the 95% confidence interval range, we conclude that $S_{opt}$ does not change with inclination in $-60° < \theta < +80°$ interval.

We further verify our suggested correlations using experimental results by Mittelmann *et al.* [1] for downward case and Starner and McManus [2] for upward inclination of 45°; these constitute all of the available inclined case data in the literature. The Mittelman *et al.* [1] data is in a very good agreement with our correlations, both Eq. (31) and Eq. (32). See Fig. 21 where the correlation curve is plotted together with the data from both Mittelman *et al.* and our simulations. The mean absolute error of Mittelman *et al.* data from Eq. (32) is only 5.8%. Such a good match with this experimental data indicates the validity of Eq. (32) in downward 60-80° range. An equivalent verification for Starner and McManus [2] data is depicted in Fig. 22. This experimental data falls in ($Gr'\,Pr\cos\theta < 250$) range. Therefore, the comparison is made with Eq. (30). Although the number of available data points is small, the data cover most of the range. The data agree very well with the correlation, yielding a mean absolute error of 8.8%. Note that both Mittelman *et al.* [1] and Starner and McManus [2] data are obtained for very different geometric parameters and conditions than both each other's and ours. Thus, their agreement with our correlation set is an indication of the generality of our suggested correlations.

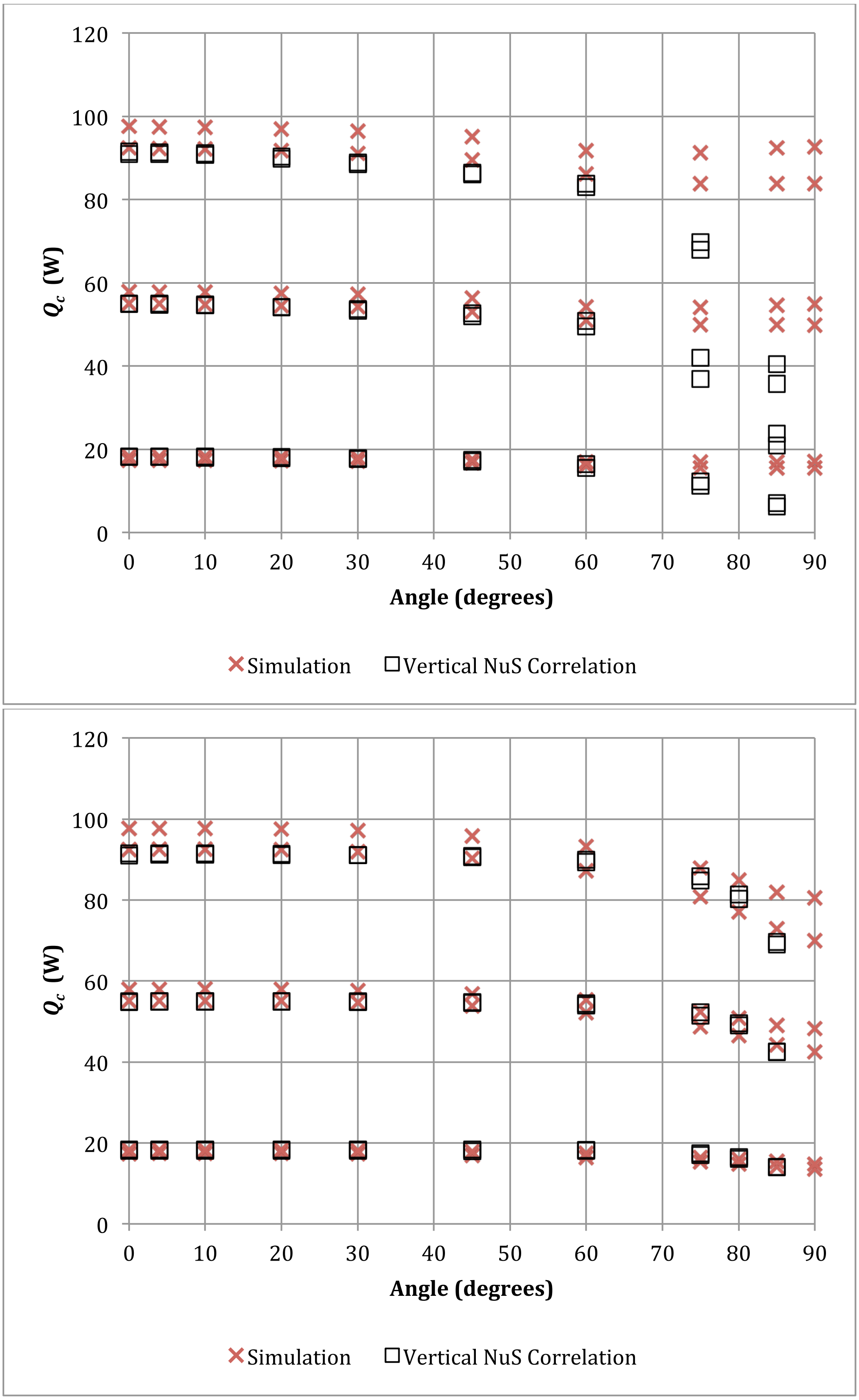


Fig. 19. Comparison between convection heat transfer rates obtained by simulation and vertical $\overline{\boldsymbol{Nu_S}}$ correlation, Eq. (32), in upward (top) and downward (bottom) inclinations for $H$=15 and 25 mm.

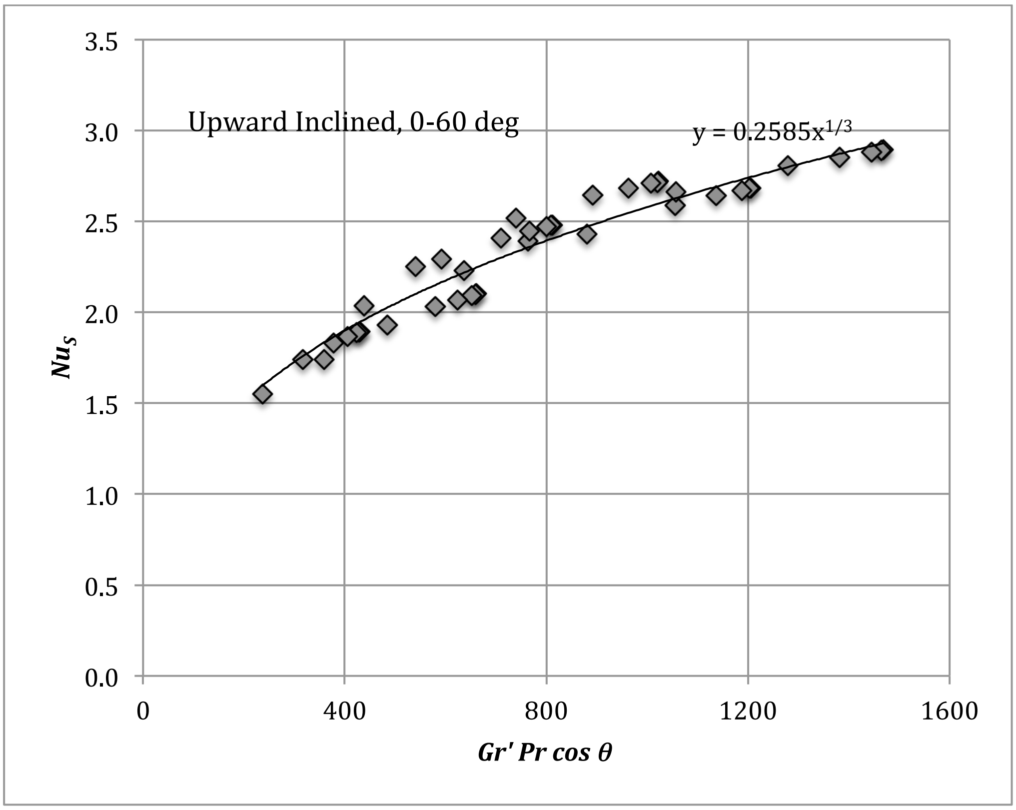


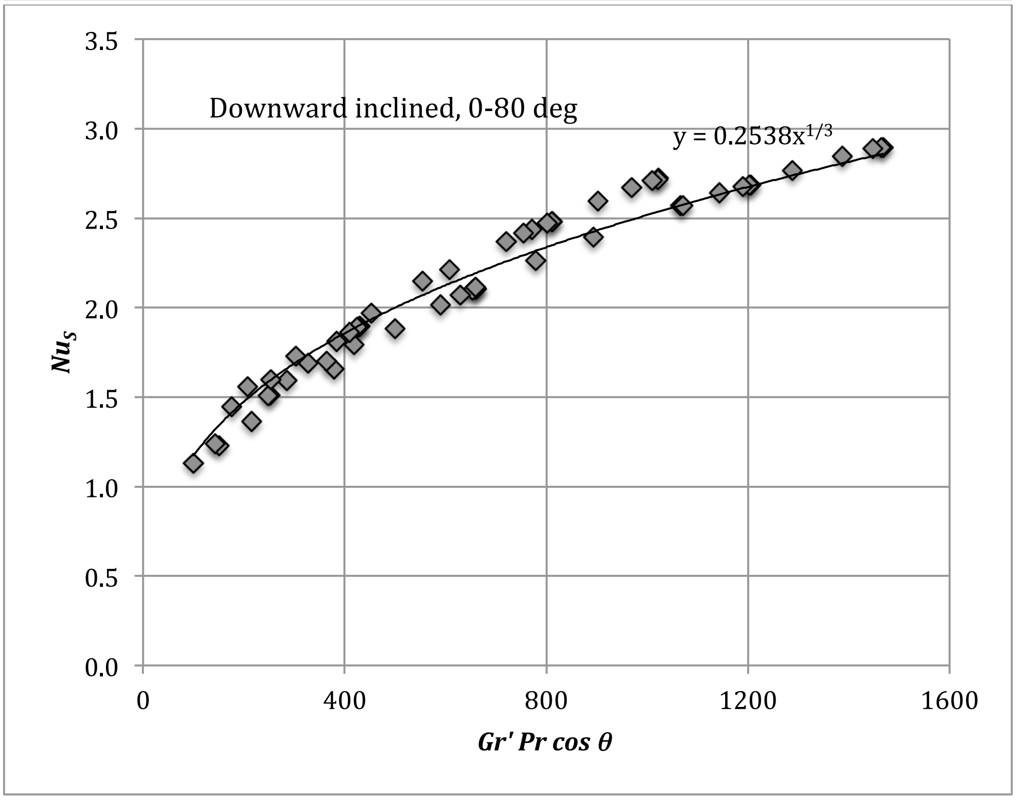


Fig. 20. Upward (top) and downward (bottom) curve fits to simulation results for angles in 0°-60° and 0°-80° ranges, respectively, and for $H$=15 and 25 mm.

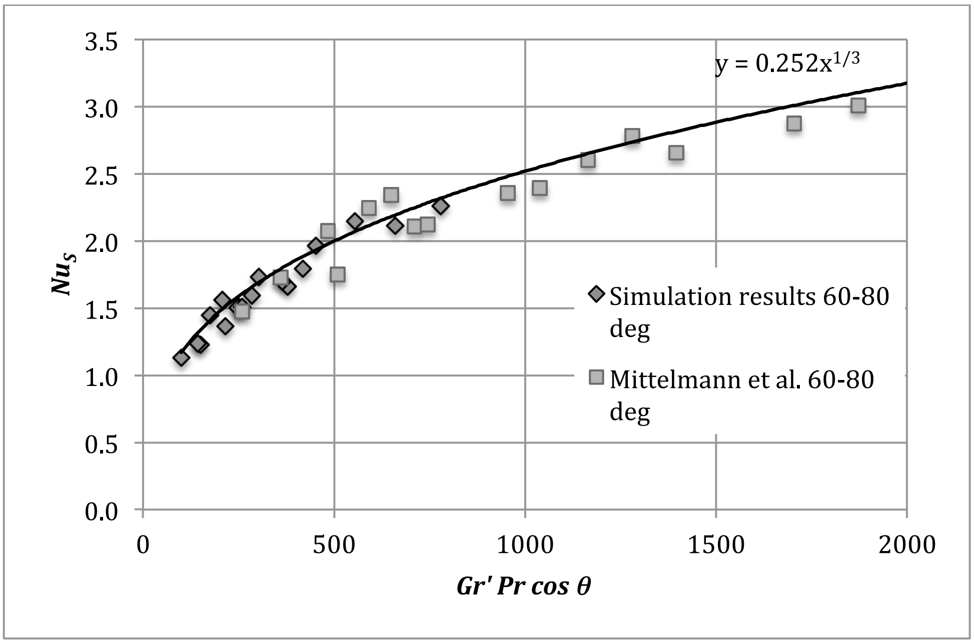


Fig. 21. Simulation results and Mittelman *et al.* [1] results in downward 60°-80° inclination angle range plotted together with Eq. (32). Agreement is very good.

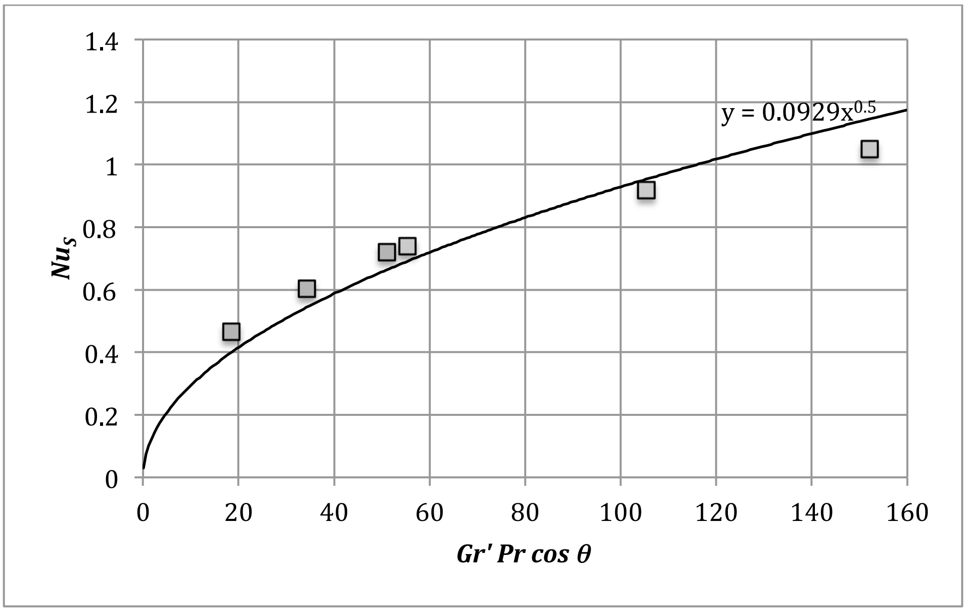


Fig. 22. Starner and McManus [2] results at -45° plotted together with our correlation in $Gr'\,Pr\cos\theta < 250$ range, Eq. (30).

*3.12 Importance of flow separation location*

For inclined flat plates, Fujii and Imura [26] have shown the validity of vertical case correlations with the $\cos\theta$ modification up to 45°. Later, Bejan and Kraus [27] recommended the cosine modification up to 60°. For plate-fin correlations, however, there is no work examining validity of the cosine modification.

In the case of upward inclinations of our plate-fin heat sink, we observe that the modified vertical correlations are valid up to 60°. For the downward inclinations, the validity range is even larger. This difference between upward and downward inclinations deserves a discussion:

Let us consider one of the channels bounded by two adjacent parallel plate fins and the base of the heat sink. The side of the channel facing the room is open. It was observed that in the vertical case, there is air inlet to the channel from the open side throughout the length (Fig. 15a). This cooler air inlet enhances the convective heat transfer rate. As shown in Fig. 15b, at -45° inclination, there is still an inlet of cool air from the open side of the channel, but the hot air exit from the upper tip of the channel is not as strong as it is in the vertical case. As the inclination angle increases in upward inclinations, we observe that hot air starts to exit from the open surface of the channel instead of the upper tip. It is observed that at -60°, flow separation is about to occur (Fig. 15c). At -75° inclination (Fig. 15d), the exit of hot air is mainly from the open side. This indicates a big change in flow structure, explaining why the cosine modification is valid up to -60° inclination. As the inclination further increases, hot air exit (separation) location moves downward from the upper tip, finally reaching to the center of the channel at -90° (Fig. 15f). The flow structure after -60° is more similar to the flow structure in the upward horizontal than the one in the vertical.

In downward inclinations, however, the phenomenon is different (Fig. 16). The flow is bounded by the heat sink at the top. When the heat sink is inclined from the vertical, air still enters the channels between the fins from the bottom and the open side of the heat sink (Fig. 16b). As the inclination increases, the entrance from the bottom gets weaker (Fig 16c). A backward circulation forms on the insulation block around +75° inclination (marked by the rectangle in Fig. 16d). This is the start of a flow separation, but it is not yet occurring on the heat sink. At +80° inclination, the separation occurs at the bottom tip of the heat sink (Fig. 16e). On the right side of the red triangle marking the flow separation, the flow is to the right and against the buoyancy force component that is parallel to the heat sink. For the separation to occur, the flow should overcome this force. This explains the delayed start of the separation (compared to the upward inclination case). As the inclination further increases, the flow separation location moves upward from the bottom tip, finally reaching to the center of the channel at +90° (Fig. 16g). The flow structure after +80° is more similar to the flow structure in the downward horizontal than the one in the vertical.

### *3.13 Inclination angles significantly deviating from the vertical*

We have demonstrated the applicability of the vertical correlation for inclination angles up to 80° for the downward case and up to 60° for the upward case.

For inclination angles significantly deviating from the vertical, the modified vertical correlations, Eqs (30)-(32), do not seem to be valid. This naturally raises the question whether the ranges 60°-90° and 80°-90°, respectively for the upward and downward cases, can be explained by horizontal models. Because our efforts are concentrated on generating a detailed validated model for the vertical case, we do not have enough data at -90° and +90° to suggest horizontal case correlations. Our limited data, nevertheless, is in agreement with the Mittelman *et al.* [1] data. The data sets align very well, Mittelman *et al.* data covering a higher $Gr'Pr$ range.

## 4. Conclusion

In the first part of the paper, we studied the natural convection from rectangular cross section vertical plate fins on a vertical base, after modeling a recent experimental set-up and conditions in [14]. We validated our numerical model by comparing the simulation results with the experimental ones. This validation forms a basis for using the model in inclined heat sink studies.

By visualizing the simulation data, we observed airflow structures within the channels formed by the fins as well as in the vicinity of the heat sink. The relation between entrance of cooler ambient air to the channels (which helps to increase convective heat transfer) and the fin height is observed from the simulation data. By visualizing temperature distributions, effectiveness of the selected base and fin thicknesses is demonstrated and the effect of fin height on the performance of the heat sink is observed. Especially at values of fin spacing significantly higher than the optimum one, the fin height affects the heat sink performance. The fin spacing is determined to be an important parameter in heat sink performance. All of these observations are consistent with the experimental literature.

Using our simulation results, we suggest the correlation in Eq. (28), via which it is possible to obtain the average Nusselt number based on the fin spacing from a modified form of Grashof number including all the geometric parameters of the heat sink. For a tighter range, $250 < Gr'Pr < 10^4$, we suggest Eq. (29). The parity plots depict the accuracy of the suggested correlations.

In the second part of the paper, we investigated the steady-state natural convection from hot heat sinks with parallel plate fins protruding from an inclined base in both upward and downward facing orientations. The examined inclination angle range includes ten angles in each orientation. As a result, the angle dependence of the phenomenon is thoroughly investigated.

It is observed that, within small inclinations from the vertical in both directions, the inclination does not reduce the convection heat transfer rate. The heat transfer rate stays almost the same. It even slightly increases in very small downward inclinations, due to thinner boundary layer.

For upward facing inclinations, we observed that the flow separation location plays an important role. Up to 60° from the vertical, the separation location stays at the top edge leading to a single flow direction in the channels between the fins. The effective body force is $\rho g\cos\theta$. The set of vertical case correlations, Eqs (28)-(29), remains valid up to 60° by multiplying the body force term with $\cos\theta$. For downward facing inclinations, the flow separation does not occur until +80°, thus, the effective body force remains $\rho g\cos\theta$ from vertical up to 80°. That is, the modified vertical case correlation remains valid in a very wide inclination angle range. Based on these observations, we suggest Eqs (30)-(32) in $-60° \leq \theta \leq +80°$.

Finally, we indirectly observed that the optimum fin spacing does not significantly change with inclinations in $-60° \leq \theta \leq +80°$ interval, indicating that optimally designed vertical heat sinks can be inclined within this range without being affected by the fin spacing.

The very good agreement of our correlations with the literature data further validates the numerical model and supports our claims. Since the investigated ranges of parameters are suitable for electronic device cooling, the suggested correlations have a practical use in electronics cooling applications.

## Acknowledgment

The work was completed and the manuscript written during a sabbatical stay of the first author at the Institute for Nanoelectronics, Technische Universität München. The first author thanks Paolo Lugli for his hospitality during that stay. He also thanks DAAD-TUM fellowship for a partial financial support. Both of the authors thank Amos Ullmann for providing their experimental data from [1] and the anonymous reviewers for their constructive comments.

## Appendix

In Table A1, we present the obtained constant coefficients $C$, 95% confidence intervals and $R^2$ values for the least squares, Tukey and Huber estimates. The selected estimates are shown in bold face.

Table A1 Coefficients, confidence intervals and $R^2$ values of power curve fits. Selected fits are marked using bold face.

| Fig. | Eq. | Least squares | | | Tukey | | | Huber | | |
|---|---|---|---|---|---|---|---|---|---|---|
| | | ***C*** | **95%CI** | ***R²*** | ***C*** | **95%CI** | ***R²*** | ***C*** | **95%CI** | ***R²*** |
| 9 | 28a | **0.0929** | **±0.0016** | **0.9607** | 0.0922 | ±0.0015 | 0.9674 | 0.0926 | ±0.0015 | 0.9661 |
| 9 | 28b | 0.216 | ±0.0046 | 0.9456 | **0.2413** | **±0.0016** | **0.9932** | 0.229 | ±0.0025 | 0.9839 |
| 10 | | **0.2301** | **±0.0049** | **0.9293** | 0.2308 | ±0.0053 | 0.9171 | 0.2314 | ±0.0054 | 0.9142 |
| 10 | 29 | **0.252** | **±0.0026** | **0.9705** | 0.2518 | ±0.0027 | 0.9664 | 0.2518 | ±0.0027 | 0.9675 |

## References

[1] G. Mittelman, A. Dayan, A. Dado-Turjeman, A. Ullmann, Laminar free convection underneath a downward facing inclined hot fin array, International Journal of Heat and Mass Transfer 50 (2007) 2582−2589.

[2] K.E. Starner, H.N. McManus, An experimental investigation of free convection heat transfer from rectangular fin arrays, Journal of Heat Transfer 85 (1963) 273−278.

[3] I. Tari, Passive cooling assembly for flat panel displays with integrated high power components, IEEE Transactions on Consumer Electronics 55 (2009) 1707−1713.

[4] I. Tari, F.S. Yalcin, CFD analyses of a notebook computer thermal management system and a proposed passive cooling alternative, IEEE Transactions on Components and Packaging Technologies 33 (2010) 443−452.

[5] W. Elenbaas, Heat dissipation of parallel plates by free convection, Physica 9 (1942) 665–671.

[6] J.R. Welling, C.V. Wooldridge, Free convection heat transfer coefficient from rectangular fin arrays, Journal of Heat Transfer 87 (1965) 439–444.

[7] C.W. Leung, S.D. Probert, Thermal effectiveness of short protrusion rectangular, heat exchanger fins, Applied Energy 34 (1989) 1–8.

[8] C.W. Leung, S.D. Probert, M.J. Shilston, Heat exchanger: optimal separation for vertical rectangular fins protruding from a vertical rectangular base, Applied Energy 19 (1985) 77–85.

[9] C.W. Leung, S.D. Probert, Natural-convective heat exchanger with vertical rectangular fins and base: design criteria, IMechE Proceedings 201 (1987) 365–372.

[10] C.W. Leung, S.D. Probert, Heat-exchanger performance: effect of orientation, Applied Energy 33 (1989) 235–252.

[11] A. Güvenç, H. Yüncü, An experimental investigation on performance of rectangular fins on a vertical base in free convection heat transfer, Heat and Mass Transfer 37 (2001) 409–416.

[12] F. Harahap, H. Lesmana, Measurements of heat dissipation from miniaturized vertical rectangular fin arrays under dominant natural convection conditions, Heat and Mass Transfer 42 (2006) 1025–1036.

[13] B. Yazicioğlu, H. Yüncü, Optimum fin spacing of rectangular fins on a vertical base in free convection heat transfer, Heat and Mass Transfer 44 (2007) 11–21.

[14] B. Yazicioğlu, Performance of rectangular fins on a vertical base in free convection heat transfer, MS thesis, Middle East Technical University, Ankara, 2005.

[15] A. Dayan, R. Kushnir, G. Mittelman, A. Ullmann, Laminar free convection underneath a downward facing hot fin array, International Journal of Heat and Mass Transfer 47 (2004) 2849–2860.

[16] Y.M. Ko, C.W. Leung, S.D. Probert, Steady-state free-convective cooling of heat exchangers with vertical rectangular fins: effect of fin material, Applied Energy 34 (1989) 181–191.

[17] H. Yüncü, G. Anbar, An experimental investigation on performance of rectangular fins on a horizontal base in free convection heat transfer, Heat and Mass Transfer 33 (1998) 507–514.

[18] H. Yüncü, M. Mobedi, A three dimensional numerical study on natural convection heat transfer from short horizontal rectangular fin array, Heat and Mass Transfer 39 (2003) 267–275.

[19] S. Baskaya, M. Sivrioglu, M. Ozek, Parametric study of natural convection heat transfer from horizontal rectangular fin arrays, International Journal of Thermal Science 39 (2000) 797–805.

[20] H.G. Yalcin, S. Baskaya, M. Sivrioglu, Numerical analysis of natural convection heat transfer from rectangular shrouded fin arrays on a horizontal surface, International Communications in Heat and Mass Transfer 35 (2008) 299–311.

[21] L. Dialameh, M. Yaghoubi, O. Abouali, Natural convection from an array of horizontal rectangular thick fins with short length, Applied Thermal Engineering 28 (2008) 2371–2379.

[22] ANSYS Fluent 12.0 Users manual, ANSYS, Inc., 2008.

[23] W.H. McAdams, Heat transmission, McGraw-Hill, New York, 1954.

[24] S.W. Churchill, H.H.S. Chu, Correlating equations for laminar and turbulent free convection from a vertical plate, International Journal of Heat and Mass Transfer 18 (1975) 1323–1329.

[25] W.H. Press, B.P. Flannery, S.A. Teukolsky, W.T. Vetterling, Numerical Recipes: The Art of Scientific Computing (3rd ed.), "Section 15.7. Robust Estimation", Cambridge University Press, New York (2007).

[26] T. Fujii, H. Imura, Natural-convection heat transfer from a plate with arbitrary inclination, International Journal of Heat and Mass Transfer 15 (1972) 755–767.

[27] A. Bejan, A.D. Kraus, Heat transfer handbook, John Wiley and Sons Inc., Hoboken, New Jersey, 2003.